Real-Time Motion Compensation in Ship-to-Ship Load Handling

Sondre Sanden Tørdal

Real-Time Motion Compensation in Ship-to-Ship Load Handling

Doctoral Dissertation for the Degree *Philosophiae Doctor (PhD)* at
the Faculty of Engineering and Science, Specialisation in Mechatronics

University of Agder
Faculty of Engineering and Science
2019

Doctoral Dissertation at the University of Agder 220
ISSN: 1504-9272
ISBN: 978-82-7117-919-9

Printed by Wittusen & Jensen
Oslo

Preface

The work presented in this doctoral thesis has been carried out in the time period starting in August 2015 and ended in October 2018 at the University of Agder, Campus Grimstad. Professor Geir Hovland from the University of Agder has been the main supervisor during the whole time.

Acknowledgments

I am sincerely grateful for the supervision provided by Professor Geir Hovland throughout the time working with this thesis. He has shown great interest in the project and has willingly shared his wisdom when most needed.

My colleagues at the University of Agder also deserve a sincere appreciation for making the University a better place to work. A special thank you goes to my colleagues Andreas Klausen and Assistant Professor Morten Ottestad which both have provided me with valuable feedback and thoughts. I also want to acknowledge my girlfriend for her patience, especially during the time of writing this thesis.

I am also grateful for the support of my family, especially my mother which always supported my choices, and for her endless belief in me.

In the end, I will acknowledge the Norwegian Education system for providing everybody with the same opportunity to fulfill and pursue an Academic degree if wanted. Without the funding and scholarships provided by the Norwegian government, this would never be possible.

Sondre Sanden Tørdal
Grimstad, Norway
October 2018

Abstract

Like the automotive industry, the maritime industry is facing a higher demand for autonomous offshore operations. It is therefore in the author's belief that the marine industry has to develop and implement new technology for both existing and new products to meet the increased autonomy demand. This thesis aims at presenting a unified understanding of the motions and the accompanying load handling issue in ship-to-ship operations. The ship-to-ship kinematics is modeled and a crane operator assistant is developed as a possible solution to increase the so-called weather window of ship-to-ship load transfers. The weather window is today determined by the significant wave height, and the current limitation of such operations is at 2.5m significant wave height. Proposing new methods capable of assisting the crane operator when transferring the load from one ship onto another is believed to further relax the weather window criteria, as well as increasing both the safety and efficiency of the operation itself.

A novel ship-to-ship estimation algorithm using the well known Extended Kalman Filter (EKF) is developed and experimentally investigated in the Norwegian Motion Laboratory. In addition to the ship-to-ship observer, an observer for measuring the suspended load motions is developed. These estimators are used to form the novel crane operator assistant presented at the end of this thesis. The presented assistant consists of a wire-length assistant and an anti-swing assistant, which both aim at assisting the crane operator in ship-to-ship load transfers by adjusting the crane operator inputs slightly in real-time. The expected outcome is increased repeatability and efficiency, as well as reduced risk in general.

The developed methods are described using a common and consistent mathematical notation for both the observers and the kinematic control systems. The appended papers at the end of this thesis have experimentally investigated and validated the proposed methods using several experiments which have been carried out in the Norwegian Motion Laboratory.

Publications

The following listed articles have been published in peer reviewed conference proceedings and journals. The versions presented in this thesis differs only in formatting compared to the published version:

Paper A S. S. Tørdal, P. O. Løvsland, and G. Hovland. Testing of wireless sensor performance in Vessel-to-Vessel Motion Compensation. In *Proceedings of the IECON 2016 - 42nd Annual Conference of the IEEE Industrial Electronics Society, Florence, Italy*, 2016. doi: 10.1109/IECON.2016.7793951.

Paper B S. S. Tørdal, and G. Hovland. Inverse Kinematic Control of an Industrial Robot used in Vessel-to-Vessel Motion Compensation. In *Proceedings of the IEEE 25th Mediterranean Conference on Control and Automation (MED), Valletta, Malta*, 2017. doi: 10.1109/MED.2017.7984313.

Paper C S. S. Tørdal, and G. Hovland. Relative Vessel Motion Tracking using Sensor Fusion, Aruco Markers, and MRU Sensors. *Journal of Modeling, Identification and Control*, 38(2):79-93, 2017. doi: 10.4173/mic.2017.2.3.

Paper D S. S. Tørdal, W. Pawlus and G. Hovland, Real-time 6-DOF Vessel-to-Vessel Motion Compensation Using Laser Tracker. In *Proceedings of the OCEANS MTS/IEEE Conference, Aberdeen, Scotland*, 2017.
doi: 10.1109/OCEANSE.2017.8084756.

Paper E S. S. Tørdal, and G. Hovland. Ship-to-Ship State Observer using Sensor Fusion and the Extended Kalman Filter. *ASME Journal of Offshore Mechanics and Arctic Engineering*, 2018. doi: 10.1115/1.4041643.

Paper F S. S. Tørdal, J. T. Olsen, and G. Hovland. The Norwegian Motion-Laboratory. *Journal of Modeling, Identification and Control*, 39(3):191-208, 2018.
doi: 10.4173/mic.2018.3.5.

In addition to the papers listed above, the following two articles were published during the time of this project. These two papers do not include the main contribution to the thesis and are therefore not attached at the end:

Paper G S. S. Tørdal, G. Hovland, and I. Tyapin, Efficient Implementation of Inverse Kinematics on a 6-DOF Industrial Robot using Conformal Geometric Algebra. *Advances in Applied Clifford Algebras*, 27(3):2067-2082, 2017. doi: 10.1007/s00006-016-0698-2.

Paper H O. Heng, and S. S. Tørdal. Calibration of the Norwegian Motion Laboratory using Conformal Geometric Algebra. In *Proceedings of the Computer Graphics International Conference (ACM), Yokohama, Japan*, 2017.w doi: 10.1145/3095140.3097285.

Contents

List of Figures

List of Tables

Chapter 1

Introduction

1.1 Motivation and Problem Statement

Ship-to-Ship load transfers have been carried out for several decades, and have played a major role in the transportation of typical cargo like bulk cargo, containers, liquefied gas, and crude oil to only mention some. Figure 1.1 illustrates the ship-to-ship operation where two supply ships are laying alongside each other and a typical container is moved to the secondary ship using the knuckle boom crane.

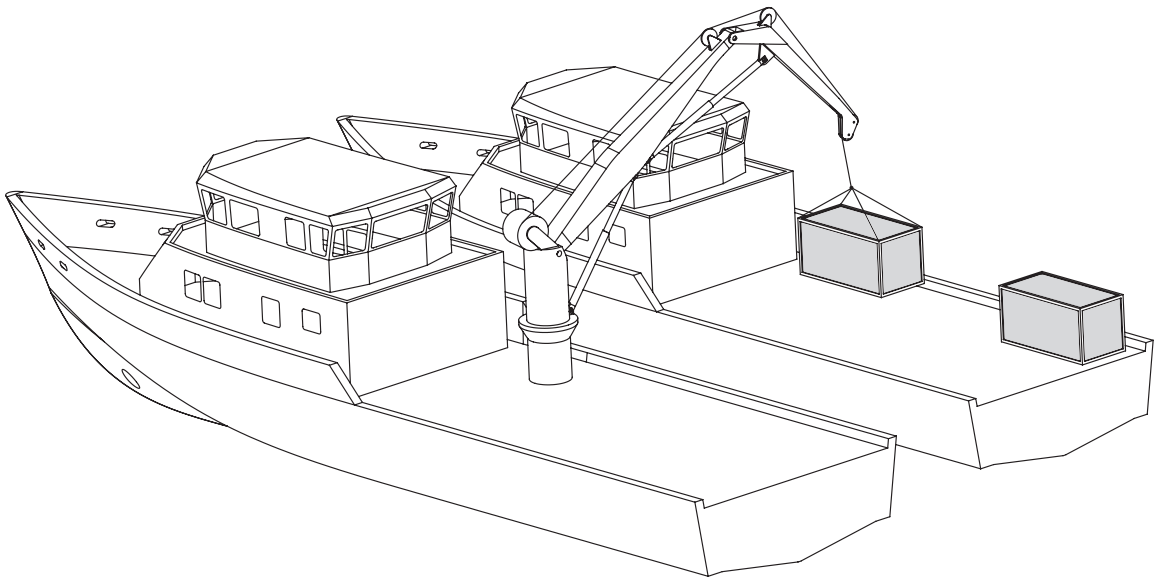

Figure 1.1: The ship-to-ship load transferring problem encountered at sea where two supply ships are laying alongside each other and the load is transferred using the knuckle boom crane.

Ship-to-ship operations are usually carried out at the open ocean, and obviously, ship-to-ship transfers reduce the need to reach the nearest port to transfer the cargo which would involve additional fuel consumption, port fees and in general longer time needed to transfer the load. Considering these factors, ship-to-ship provide both environmental and economic benefits since the operation can be carried out at open sea and no specific port is needed. On the other hand, ship-to-ship involves increased risk due to the operation itself,

and there is a need for specific personnel which is skilled to accomplish the operation. The crane operator is usually considered to carry out the most vital task in ship-to-ship transfers, since the crane has to be operated in such a manner that neither the equipment nor the personnel are harmed. This task is considered by the offshore industry to be challenging, and hence restricted to only be carried out when the significant wave height is below 2.5 meters [3]. The significant wave height is traditionally defined as the mean wave height of the highest third of the waves. This limitation is known as the weather window for such operations, and by introducing new technology there exists great potential in increasing these margins by introducing automatic or autonomous systems which can assist the crane operator in such a demanding task. As a result, reduced fuel consumption and waiting time may be achieved by relaxing the weather condition requirement.

These arguments are the main motivation to further investigate the ship-to-ship operation and hence carry out research towards developing new technology which can increase the efficiency, repeatability and the safety of such operations. Another motivational factor is that a higher level of autonomy is expected in future offshore load handling and shipping activities in general. In [4] it is stated: *Autonomous shipping is the future of the maritime industry. As disruptive as the smartphone, the smart ship will revolutionise the landscape of ship design and operations.* In other words, the offshore industry is today facing a major technological shift, where an increased autonomy level is expected in adjacent future. Like the automotive industry, the goal of accomplishing fully autonomous cars e.g. is realized through gradually introducing assisting systems like adaptive cruise control, adaptive lane assistant, and automatic emergency braking. These systems aim at assisting the driver to operate the car more efficiently and increase the driving safety. It is therefore in the author's belief that the offshore load handling industry should follow the same path to reach the goal of fully autonomous operations in the future. Hence the crane should still be operated by a crane operator, but new technology should continuously assist the operator to carry out the task with higher repeatability, efficiency, and reduced risk. This thesis aims at investigating these matters using experiments and modeling of the ship-to-ship operation to gain a more scientific understanding of the problem. The main research questions to be investigated in this thesis are:

1. Are new control algorithms and off-the-shelf sensors capable of increasing both the efficiency and safety of ship-to-ship operations?

2. Can a payload anti-swing solution for ship-to-ship transfer be developed and demonstrated using proprietary industrial control systems?

3. Can new technology like a crane operator assisting system contribute to further increase the weather window of ship-to-ship transfers?

1.2 Thesis Outline

This thesis is divided into three main chapters, which in the end are accompanied by the appended papers listed in the beginning. The content of each chapter is briefly summarized in the following:

Chapter 1 - Introduction

This chapter presents the problem to be investigated and the accompanying research motivation for this project, followed by a brief outline of the thesis (this one) aimed at giving the reader an outlook of the content to be discussed and presented throughout the thesis. The current state-of-the-art is briefly summarized, where the focus lies on the current offshore sensor and motion compensation technologies. In the end of the introduction, a summary of the appended papers is given, and the main contributions of this project are summarized.

Chapter 2 - Background Theory and Modeling of Ship-to-Ship Operations

This chapter aims at presenting a unified theory of the work presented throughout the appended papers. The chapter begins with defining the ship-to-ship problem in a geometrical sense and hence both the crane and the ship-to-ship kinematics are modeled. In the end, a crane operator assistant is presented which aims at combining all the work conducted in the appended papers with an anti-swing system.

Chapter 3 - Concluding Remarks

In the end, the outcome of this project is discussed and some concluding remarks are given. In addition, further work is briefly discussed, where ideas and possible improvements are discussed.

Appended Papers

All the previously listed papers are included at the very end of this thesis, and the reader is encouraged to go through the appended papers to gain more details about the experiments which have been conducted throughout the project.

1.3 State-of-the-Art

This section presents some of the current state-of-the-art applications which are related to offshore load handling operations. Most of the current state-of-the-art applications are obviously found in the offshore load handling industry, and some of the largest companies delivering offshore load handling equipment are; MacGregor Norway AS, Barge Master, National Oilwell Varco (NOV), Palfinger and Libherr. This section will briefly elaborate on the four most relevant technologies related to ship-to-ship motion compensation; the Active Heave Compensated (AHC) crane, the 3D compensated crane, ship-to-ship load transfers, and the anti-swing control for cranes.

1.3.1 Active Heave Compensated Crane

The current state-of-the-art within the branch of offshore load handling is the AHC crane. This technology is featured by all the previously mentioned offshore crane manufacturers. Figure 1.2 illustrates a typical offshore knuckle boom crane which is usually equipped with the AHC technology.

Figure 1.2: An offshore AHC knuckle boom crane manufactured by MacGregor [1].

AHC is used to decouple the ship motion from the suspended load in the heave direction, which makes it much easier to land the cargo on fixed installations or onto the seabed. The winch is usually utilized to continuously adjust the wire length based on the measured heave position and velocity of the ship such that the cargo does not move compared to a stationary surface. The ship motion is determined by one or several Motion Reference Units (MRUs). An MRU utilizes information from an accelerometer and a gyroscope to determine the motion of the ship in real-time. Various types of filtering techniques are implemented in the MRU software to make the output more precise and reliable. These filters reduce the drift in the position output due to the double integration of the measured ship acceleration in the gravity direction. The drift is usually caused by non zero noise in the sensors and hence the topic has gained a lot of interest both in the academia and the industry. Kongsberg Maritime/SEATEX is considered to deliver the current state-of-the-art MRU unit which also is considered the de facto standard MRU unit for AHC cranes. Kongsberg/SEATEX utilize their own adaptive heave filter [5], while other filtering approaches have been investigated in the academia [6, 7, 8, 9].

In addition to the AHC crane, both passive and hybrid active-passive compensation systems exist as described in [10]. Furthermore, several publications related to various methods towards increasing the accuracy and effectiveness of the heave compensation problem are published in [11, 12, 13, 14, 15].

1.3.2 3D Compensated Cranes

The AHC crane previously mentioned is only capable of compensating for the ship heave motion using the winch, meaning that changes in the attitude of the ship will cause the crane tip to move, which again cause the load to swing. This continuously swinging makes the maneuvering of the crane even more complicated, and hence the offshore industry has recently made an attempt to solve this problem by introducing a new branch of cranes capable of also compensating for the roll and pitch angles of the ship. Both MacGregor

and Barge Master offer such cranes today, and the two types are the MacGregor 3D crane [16] and the Barge Master T-40 [17]. These cranes can transfer loads in a much more controlled manner since the tower of the crane is always kept in a vertical position and hence the load is less prone to swing motion due to reduced crane tip motion. These products are however not mature and require a complicated actuation system capable of moving the crane tower in a vertical position at all times using the measured roll and pitch angles acquired by an MRU. The Barge Master T-40 crane is shown in Figure 1.3.

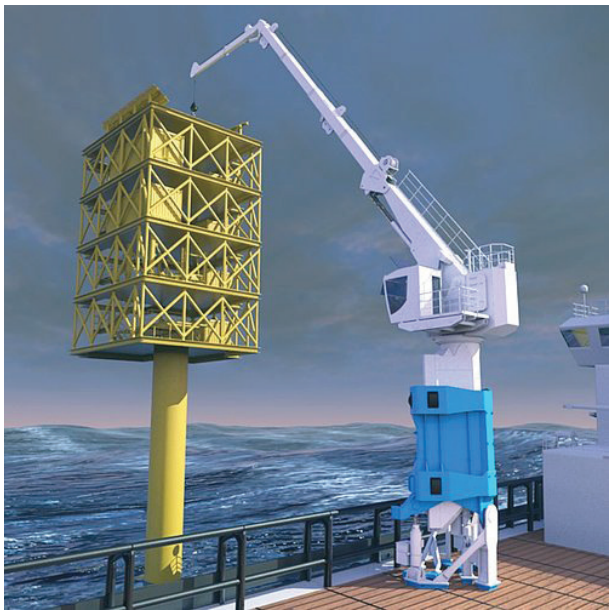

Figure 1.3: The 3D compensated crane delivered by Barge Master which is capable of compensating for roll, pitch and heave motions up to 3m significant wave heights [2].

1.3.3 Ship-to-Ship Load Transfer

During the time of working with this project, which is part of the Norwegian SFI Offshore Mechatronics research center[1], both the SFI parters MacGregor and NOV have released new products related to ship-to-ship load transferring using two MRUs and a wireless link to actively control the load to follow the ship deck of the second ship in real-time, see [18] and [19]. These systems are capable of compensating the heave motion of both the ships using the winch. In these solutions both the roll and pitch motions of the ships are neglected, which also should be considered when trying to land the load on the second ship deck. However, it is worth mentioning that both these products were released after the first publication of this project (Paper A). This paper experimentally investigated the use of two MRUs combined with a low latency radio link to carry out the ship-to-ship compensation in real-time.

The ship-to-ship problem has gained increased interest within the offshore industry, but academic research toward solving this problem is limited, and unfortunately not to be considered very mature. The only academic papers found which are directly related to the ship-to-ship operation are [20] and [21]. These papers mainly focus on the hydrodynamic

[1]Center for Research Based Innovation Offshore Mechatronics `https://sfi.mechatronics.no/`

interaction forces occurring in-between the ships during the operation and not the load transfer problem. However, there exist literature related to best practice and guides related to ship-to-ship transfers in [22] and [23]. In addition, various ports have defined regulations related to ship-to-ship transfers like the one given by the port of Gothenburg in [24]. Finally, patents related to transfer of fluids [25] and a refueling device [26] are found when searching for ship-to-ship transfer literature.

1.3.4 Crane Anti-Swing Control

Anti-swing control is supposed to dampen out the swinging motion of a suspended load, and hence increase the operational efficiency, repeatability, and safety in moving the transported load. A listing of the current available commercial anti-swing systems for overhead industrial cranes is found in [27]. The sliding mode control approach for dampening the suspended load swing motion has been investigated for overhead cranes in [28] and [29]. Offshore crane related studies are given in [30] and [31] where numerical time-domain simulations were used to verify the effectiveness of the proposed control algorithms. Partial feedback linearization for an overhead crane was experimentally investigated using a small scale test setup in [32] and finally an energy based controller was derived using the Lyapunov technique in [33].

The research mentioned so far in relation to the anti-swing control problem is considered to be dominated by modern control theory, where the problem is solved by using accurate mathematical models of the plant, and hence the control input relies on observing the plant with high accuracy. However, the results published in [34] represent a more realistic approach to solve the problem where an offshore crane is considered instead of the industrial overhead cranes. Based on the recent research the author believes that future research toward anti-swing controllers applied to industrial knuckle boom cranes is needed to meet the future demands of autonomy in offshore operations, especially where the crane base is moving due to the ocean waves and wind influencing the ship.

1.4 The Norwegian Motion Laboratory

The experiments in this project are carried out in the Norwegian Motion Laboratory located at the University of Agder, Campus Grimstad. This section aims at giving the reader a brief overview of the lab setup and the accompanying development phases carried out throughout this project. For a more detailed description related to the lab setup, the reader is referred to Paper F which discusses the lab setup more thoroughly. The lab consists of several machines and sensors, and to gain an overview of the lab, Figure 1.4 illustrates the lab setup found in the Norwegian Motion Laboratory.

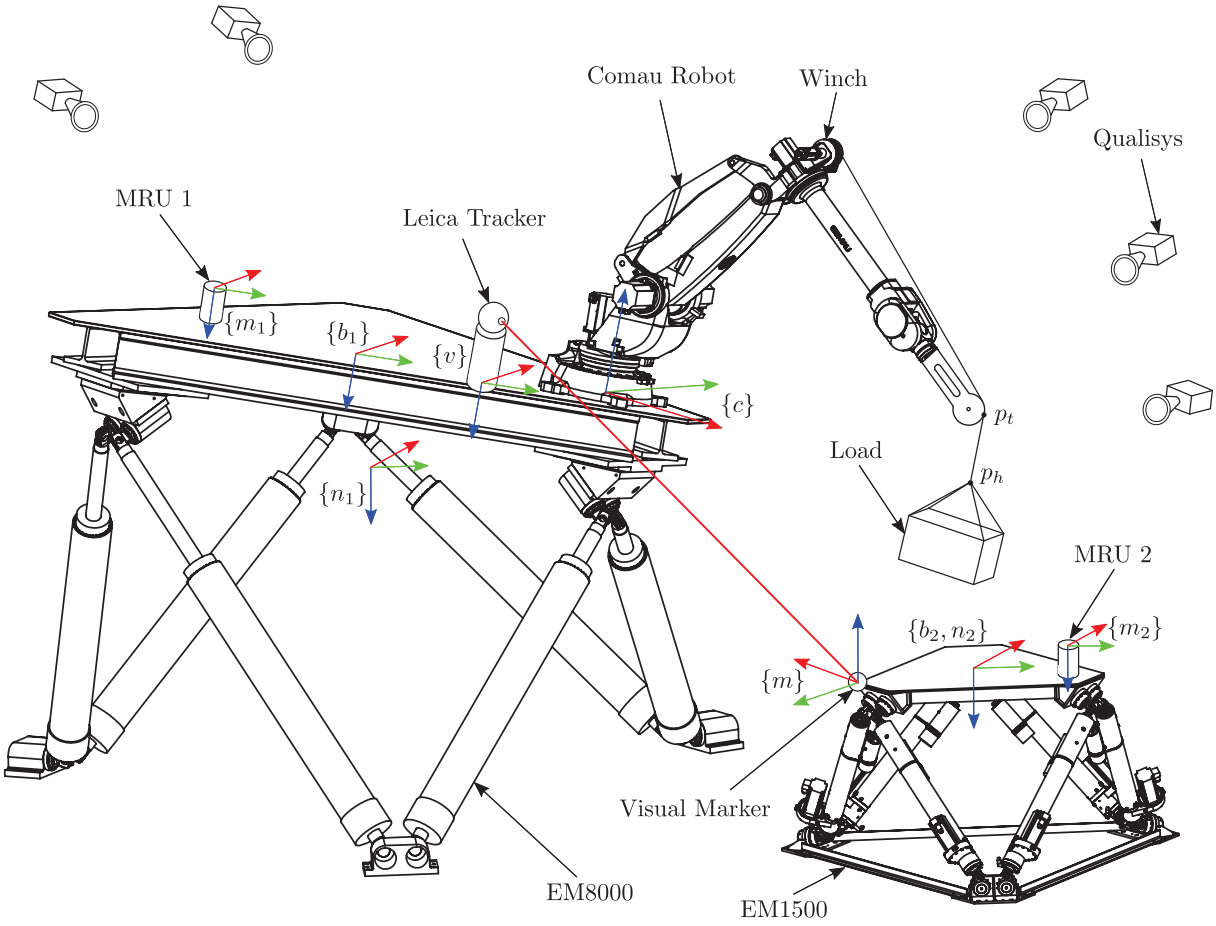

Figure 1.4: Schematic overview of the Norwegian Motion Laboratory, where the coordinates of both the machinery and sensory equipment are named according to Table 1.1.

Figure 1.4 illustrates the lab setup and the coordinate systems of both the sensory and the robotic machines used throughout the project. $\{\cdot\}$ is used to denote a coordinate system, and Table 1.1 defines each of the coordinate systems and their respective representation.

Table 1.1: The coordinate systems used to describe the geometry of the machines and sensors found in the lab setup.

Symbol	Description
$\{n_1\}$	Neutral pose of EM8000.
$\{n_2\}$	Neutral pose of EM1500.
$\{b_1\}$	Body coordinate of EM8000.
$\{b_2\}$	Body coordinate of EM1500.
$\{m_1\}$	Motion Reference Unit (MRU) mounted on EM8000.
$\{m_2\}$	MRU mounted on EM1500.
$\{c\}$	Comau robot base coordinate system.
$\{v\}$	Coordinate system of the Leica AT960 laser tracker.
$\{m\}$	Leica T-Mac TMC30 tracking probe placed on EM1500.

In addition to the coordinate systems, the wire exit at the tool point is named $\boldsymbol{p}_t$ and the hook connecting the wire and the suspended load is named $\boldsymbol{p}_h$. The Qualisys motion capture system is not represented with a separate coordinate system $\{q\}$ since it is calibrated to measure relative to coordinate $\{v\}$ i.e.

$$\{q\} = \{v\}. \tag{1.1}$$

A common control interface had to be developed in order to control and monitor all the equipment found in the lab. Each of the machines and sensors have their own proprietary interface, and a central control unit was used to interface each of them. The central control unit is manufactured by Beckhoff and the specific unit is named CX2040. The reason for using this embedded PC is motivated from the several capabilities and flexibility of interfacing various types of machines and sensors. In addition, Beckhoff has their own servo drives which are used to realize the winch on top of the robot. Figure 1.5 illustrates the communication layout used to interface the central control unit with all the equipment.

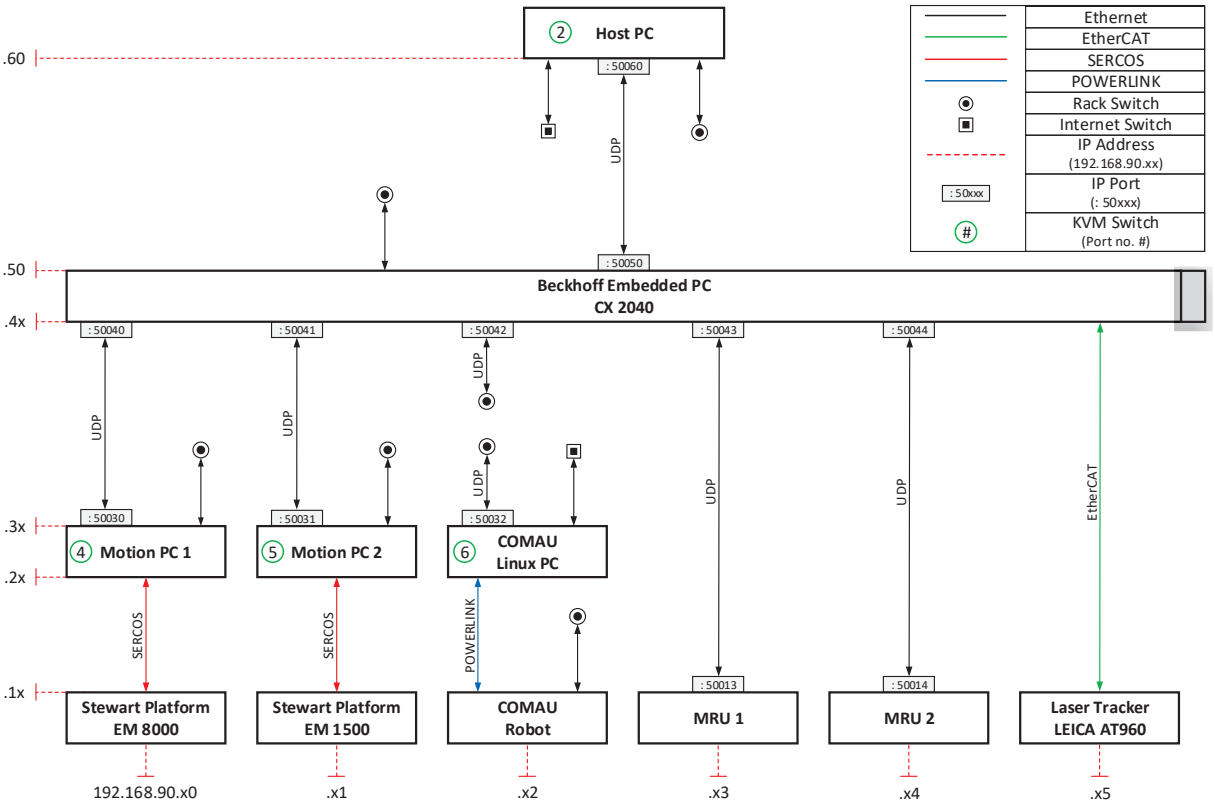

Figure 1.5: The communication interface inherited from Paper F which is used to illustrate all the connections used to monitor and operate the Norwegian Motion Laboratory in real-time.

As the figure illustrates, extensive work is carried out to develop the laboratory into its current state. A Gantt chart is used to show the various development phases in comparison to the publication date of the appended papers.

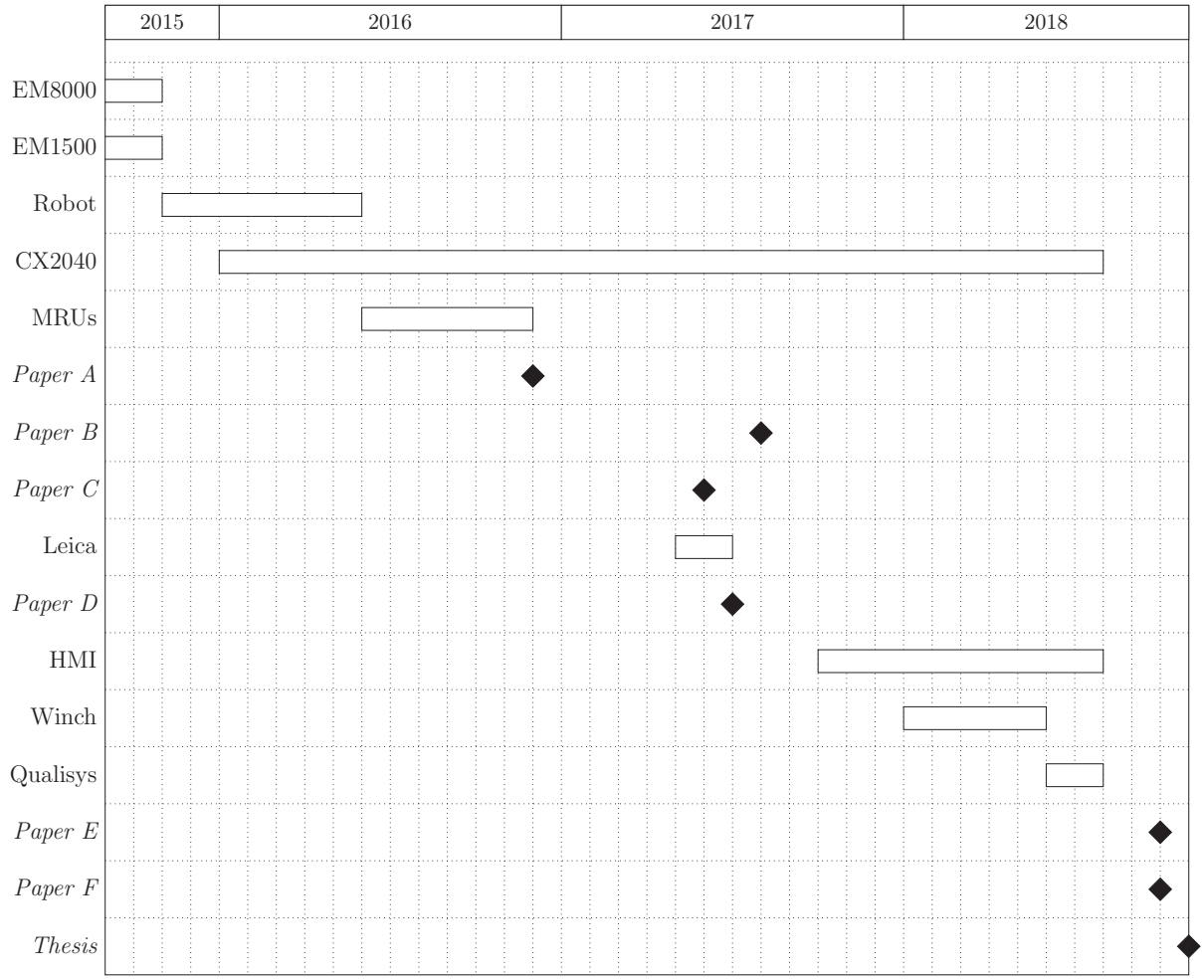

Figure 1.6: Lab development phases in comparison to the date of publication of the appended papers.

1.4.1 Control Limitations

Industrial machines like the ones found in the lab are usually equipped with a proprietary controller and an accompanying software interface, which implies that the inner control control loops are already developed and only some parameters can be adjusted by the user. Integrating such machines in a system setup like the one found in the Norwegian Motion Laboratory introduces some challenges due to the lack of full control of the inputs to the machines, where some of the main challenges are:

- The machines are meant to be operated on a point-to-point basis, meaning that the user commands the machines to move from A to B and the software will interpolate the motion and execute the motion according to some predefined settings for the maximum velocity and acceleration.

- Continuous operation of the machine will require the user to generate a trajectory for the position, velocity and acceleration which do not violate the maximum allowable deviations. This often implies that no step inputs are allowed, which may be required to identify the system dynamics.

- The user can not operate the machine using torque/force inputs which is often the input to be controlled when analyzing the control problem using classical control theory methods.
- The system dynamics can be hard to describe or identify due to the unknown control structure and parametrization already implemented in the control software.

On the other hand such machines offer the following benefits compared to designing the whole control system from scratch:

- Easier operation for non-control experts is achieved by using the already implemented software which only accepts certain types of inputs.
- The software will ensure that the machine is not overloaded and destroyed due to wrong use of the machine.
- The machine is implemented by a software interface only, meaning that a full dynamic analyses and control system development is not required to have a functional machine.

These considerations have to be considered when designing state estimation and control algorithms for the system integration task, and hence the focus throughout the thesis has heavily relied on the kinematic study and not detailed dynamic modeling of the control task. This means that a mathematical framework describing the kinematics is mainly used to generate correct reference inputs for the already existing proprietary control systems using the available sensor data. Such and approach is known as kinematic control where the task is typically defined to design a high level controller to achieve the desired robot motion.

1.4.2 GitHub Repository

A major part of this project has been devoted to programming in different languages including Python, Structured Text, Matlab/SIMULINK, and C/C++. Instead of appending all the code as a textual appendix, a GitHub library containing all the code which is used to build the common control interface, the Human Machine Interface (HMI), and the accompanying algorithms are made available online. The Motion Laboratory GitHub repository is found at `https://github.com/sondre1988/motion-lab` and is open for everyone to use according to the license stated inside the repository. The easiest way to clone the repository is to download and install Git for your specific OS and then execute the following command:

```
git clone https://github.com/sondre1988/motion-lab
```

1.5 Summary of Papers

Paper A - Testing of Wireless Sensor Performance in Vessel-to-Vessel Motion Compensation

Summary: This paper presents two physical experimental setups aimed at verifying the possibility of using a wireless communication link in combination with a second MRU to measure the heave motion of the second ship in real-time. The main experiment was carried out in the Norwegian Motion Laboratory using both Stewart platforms to simulate two offshore vessels/ships laying alongside each other, and the industrial robot was used to simulate the load handling crane used to compensate for the relative heave motion. A high precision laser tracker was used to measure the overall compensation performance when two MRU sensors were used to measure the motion of the two Stewart platforms while the second MRU data was transmitted wirelessly. In addition to the indoor experiment, an outdoor experiment was conducted to determine the typical time delay when the wireless transmitters were placed at a distance of 70 m away from each other. For a test duration of 24h, 6,813,448 data packages were continuously transmitted, and the time delay for each package was measured and logged to a histogram. The typical time delay was found to be 8ms, which in the end led to the conclusion that this delay would not affect the overall performance due to the slow ship motions.

Contributions: Wirelessly transmitted MRU signals applied to the ship-to-ship problem were experimentally investigated using two experimental setups. The resulting transmission delay was found to be typically 8ms and hence proved to be a possible solution to the problem of measuring the relative ship heave motion using two MRUs. At the time of conducting these experiments, the proposed idea was considered novel, and it is worth mentioning that the industry has published products using this technology after the acceptance of this paper.

Published as: S. S. Tørdal, P. O. Løvsland, and G. Hovland. Testing of wireless sensor performance in Vessel-to-Vessel Motion Compensation. In *Proceedings of the IECON 2016 - 42nd Annual Conference of the IEEE Industrial Electronics Society, Florence, Italy*, 2016. doi: 10.1109/IECON.2016.7793951.

Paper B - Inverse Kinematic Control of an Industrial Robot used in Vessel-to-Vessel Motion Compensation

Summary: The work presented in this paper should be seen as an extension of the work presented in Paper A where the motion compensation algorithm was extended to also compensate for the roll and pitch motions of both the Stewart platforms representing the two ships. The relative kinematics between the two ships have been modeled using homogeneous transformation matrices which are used to calculate the required kinematic motion of the industrial robot due to the asynchronous motions simulated by the two Stewart platforms. The resulting accuracy was measured by the high precision internal feedback sensors of the robotic equipment featured by the Motion Laboratory which is calibrated using a high precision laser tracker according to Paper H. In addition to the experimental work, the need for a third sensor capable of a measuring/calibrating the off-

set parameters between the two inertial coordinate systems of the two MRUs was stated.

Contributions: The maximum compensation error was measured to be 42 mm, which again proved the possibility of using an MRU combined with a wireless MRU as a possible solution to the ship-to-ship/vessel-to-vessel problem. However, the paper claims the need for a third sensor to measure/calibrate the inertial offset between the two MRUs, which has led to further investigation of this matter in the next papers.

Published as: S. S. Tørdal, and G. Hovland. Inverse Kinematic Control of an Industrial Robot used in Vessel-to-Vessel Motion Compensation. In *Proceedings of the IEEE 25th Mediterranean Conference on Control and Automation (MED), Valletta, Malta*, 2017. doi: 10.1109/MED.2017.7984313.

Paper C - Relative Vessel Motion Tracking using Sensor Fusion, Aruco Markers, and MRU Sensors

Summary: This paper presents a possible solution to the issue of measuring the inertial offset between the two MRUs. Paper A and B demonstrated that the MRUs are accurate enough to be used in ship-to-ship load handling, but a third sensor is needed to measure or calibrate the inertial offset between the MRUs in real-time. A sensor fusion algorithm incorporating the use of several visual fiducial markers and two MRUs was experimentally investigated, where a vision system was used to measure the inertial offset. The second MRU was placed inside a cube where five Aruco markers were placed on each of the cube sides to enable for the visual tracking application to measure the cube motion relative to the main Stewart platform. The acquired sensor measurements were fused together to estimate the relative Stewart platform motions in real-time. The cube was placed onto several locations on the second Stewart platform, and the proposed system proved to be self-calibrating, meaning that no manual work had to be carried out when the cube was placed in several arbitrary locations.

Contributions: A novel approach to fuse two MRUs and visual tracking of multiple Aruco markers placed on a cube was used to develop a self-calibrating system which intends to measure the relative ship motions in real-time. The system proved to be self-calibrating, and the standard deviation of the motion compensation task was found to be 31 mm.

Published as: S. S. Tørdal, and G. Hovland. Relative Vessel Motion Tracking using Sensor Fusion, Aruco Markers, and MRU Sensors. *Journal of Modeling, Identification and Control*, 38(2):79-93, 2017. doi: 10.4173/mic.2017.2.3.

Paper D - Real-time 6-DOF Vessel-to-Vessel Motion Compensation Using Laser Tracker

Summary: The previous paper relied on the use of MRU sensors to measure the relative ship motions in combination with a third sensor. This paper aims at investigating the use of only one state-of-the-art laser tracker and compare the results with the previously published papers of this project. The laser tracker was manufactured by Leica, and the specific model is the AT960 which is capable of tracking 6 degrees-of-freedom in real-time using the accompanying T-Mac TMC30 tracking probe. The hand-eye calibration problem often encountered in robotics proved to be useful in the sense of calibrating the lab setup, and the calibration errors were discussed accordingly. The resulting ship-to-ship motion tracking proved to be superior in comparison with previously published results, but the method suffers from less reliability due to lack of redundancy and the need for visual sight at all times.

Contributions: A state-of-the-art tracking accuracy in ship-to-ship pose estimation was achieved using a high precision laser tracker manufactured by Leica. However, the proposed method lacks redundancy and hence is less suitable for harsh offshore environments where sea spray, obstacles and fog may interrupt the visual sight of the laser tracker during operation.

Published as: S. S. Tørdal, W. Pawlus and G. Hovland, Real-time 6-DOF Vessel-to-Vessel Motion Compensation Using Laser Tracker. In *Proceedings of the OCEANS MTS/IEEE Conference, Aberdeen, Scotland*, 2017.
doi: 10.1109/OCEANSE.2017.8084756.

Paper E - Ship-to-Ship State Observer using Sensor Fusion and the Extended Kalman Filter

Summary: This paper aims at presenting a unified theory for estimating the relative motion between two ships lying alongside each other using the EKF to combine both visual and inertial sensors in real-time. The ship-to-ship estimation problem is modeled using a pure kinematic model, meaning that no physical ship parameters were included. Adding the physical ship parameters would most likely increase the estimation performance but was left out since it was assumed that these parameters are hard to achieve or estimate. Measurement models used to fuse the measurements of two MRUs and the laser tracker presented in Paper D were derived. The Motion Laboratory was utilized to experimentally investigate the estimation performance using the developed EKF algorithm. The developed EKF algorithm is also capable of handling interrupted visual sight for small time periods, meaning that estimation redundancy was introduced to the solution by using only the two MRUs for smaller time periods. The tracking performance was reduced when the laser tracker lost sight, but not to such an extent that the ship-to-ship transfer would be impossible.

Contributions: A redundant sensor fusion algorithm aimed at estimating the relative

motions between two ships at sea was developed and experimentally tested to verify the estimation effectiveness and accuracy. The sensor fusion algorithm was developed using the EKF and used to combine two MRUs, and a laser tracker in real-time. The redundancy was proved to be functional due to the possibility of losing the visual sight of the laser tracker for a time duration of 50s in the middle of the test sequence.

Published as: S. S. Tørdal, and G. Hovland. Ship-to-Ship State Observer using Sensor Fusion and the Extended Kalman Filter. *ASME Journal of Offshore Mechanics and Arctic Engineering*, 2018. doi: 10.1115/1.4041643.

Paper F - The Norwegian Motion-Laboratory

Summary: Throughout all the appended papers of this thesis, the Norwegian Motion Laboratory has played a major role in realizing all the experiments used to validate the developed methods for the ship-to-ship load transfer problem. At the time of starting this project, the lab facility consisted of mainly two Stewart platforms, and the industrial robot without any common control interface. Extensive further development of this lab was therefore needed to conduct the required experiments presented in this thesis. This paper aims at presenting and documenting the lab facility in terms of; the common control interface, the open-source PyQt HMI interface, the calibration of the lab setup, the kinematics and geometrical descriptions of the equipment, summary of all the sensors and limitations of the lab equipment in general, and finally list a brief summary of previous research activities carried out in the lab to date.

Contributions: Extensive development of a common control interface capable of interfacing all the sensors and operate all the robotic equipment from a single main control unit in real-time. A GitHub library containing all the developed code is made publicly available for further development of the lab, or for others to gain insight and possible reuse code for their own projects in the future.

Published as: S. S. Tørdal, J. T. Olsen, and G. Hovland. The Norwegian Motion-Laboratory. *Journal of Modeling, Identification and Control*, 39(3):191-208, 2018. doi: 10.4173/mic.2018.3.5.

1.6 Contributions

The goal of the work presented in this thesis has been to develop and implement new ideas, methods, algorithms and software which could potentially be used in industrial practice in nearby future. A list of the main contributions is given below:

- Investigation of wireless MRU data transfer for offshore use.

- Development and study of the system kinematics related to the ship-to-ship motions, the motion of the crane, and the suspended load motion during ship-to-ship transfers.
- Experimental investigation of combining inertial and visual sensors in ship-to-ship state estimation utilizing the well established EKF algorithm.
- Development and experimental testing of an anti-swing system for a crane with a moving base using a Linear Quadratic Regulator (LQR) state feedback. The proposed method is supposed to be modular in the sense that it can be integrated with an already existing proprietary crane controller.
- Modeling and real-time kinematic control of a suspended load transferred from one ship onto another using an offshore crane and the accompanying winch.
- Extensive further development of the experimental lab setup known as the Norwegian Motion Laboratory.

Chapter 2

Background Theory and Modeling of Ship-to-Ship Operations

2.1 Geometric Definitions

Throughout this project, extensive investigation of the kinematics of the crane, ship-to-ship body postures and the motion of the transferred load are investigated in order to gain a more scientific understanding of the problem. Figure 2.1 presents an overview of the ship-to-ship operation which will be modeled and discussed throughout this chapter.

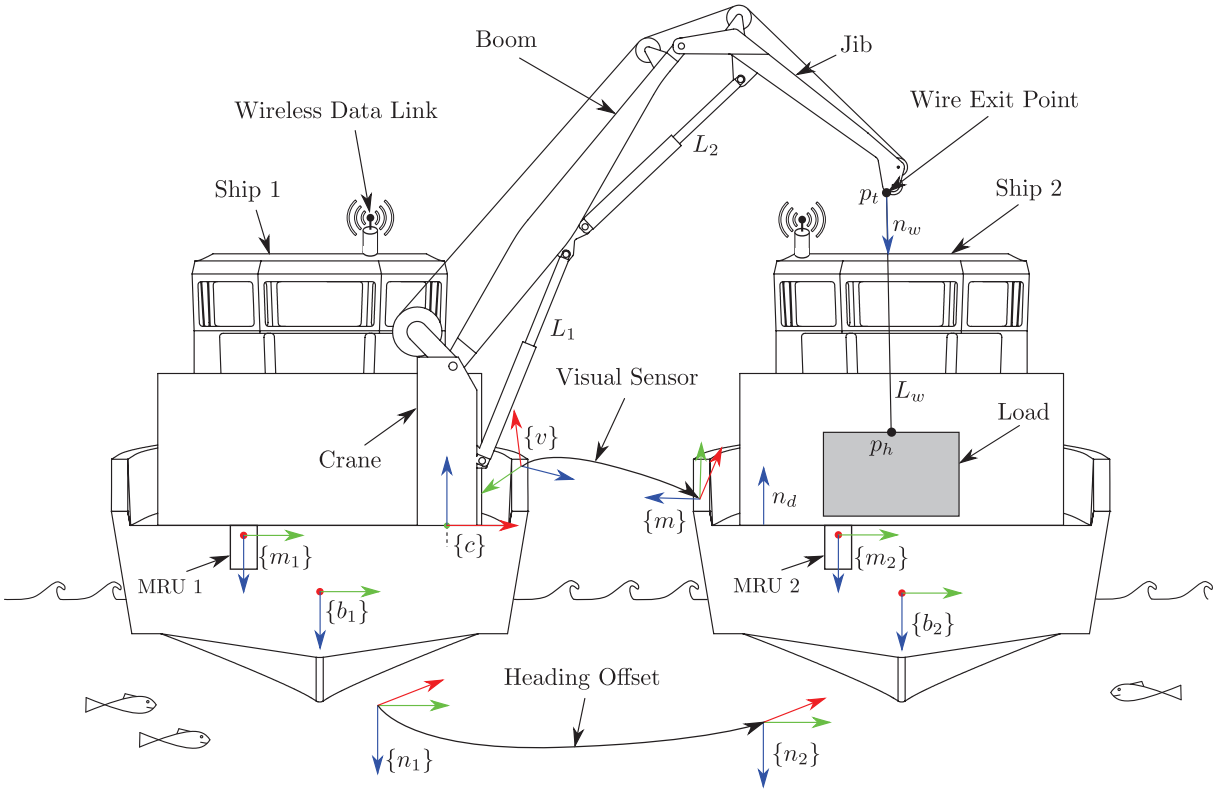

Figure 2.1: The different coordinate systems involved during ship-to-ship operations.

The figure illustrates the two ships laying alongside each other at sea, and hence the offshore load handling crane is used to transfer the load from the main ship onto the

secondary ship. The coordinate systems are denoted using the bracket notation $\{\cdot\}$ where the name of the specific coordinate system is $\cdot$. This naming will be frequently used in forming the kinematic equations describing the spatial body motions throughout the whole chapter. Section 2.2 will discuss the notation more carefully, and hence the reader is encouraged to read this section. Table 2.1 summarizes the annotations seen in Figure 2.1 and presents a brief description of each of the symbols.

Table 2.1: Table describing the kinematic definitions presented in Figure 2.1.

Symbol	Description
$\{n_1\}$	Heading coordinate system 1.
$\{n_2\}$	Heading coordinate system 2.
$\{b_1\}$	Coordinate system at Center of Gravity (CG) of ship 1.
$\{b_2\}$	CG of ship 2.
$\{m_1\}$	Motion Reference Unit (MRU) mounted on ship body 1.
$\{m_2\}$	MRU mounted on ship body 2.
$\{c\}$	Crane base coordinate system.
$\{v\}$	Coordinate system of the visual sensor placed on ship 1.
$\{m\}$	Coordinate system of the visual marker placed on ship 2.
L_1	Length of crane cylinder actuating the main boom.
L_2	Length of second cylinder actuating the crane jib.
L_w	Wire length between points $\boldsymbol{p}_t$ and $\boldsymbol{p}_h$.
$\boldsymbol{p}_t$	The crane tip point where the Wire Exit Point (WEP) is located.
$\boldsymbol{p}_h$	The point where the hook is connected to the transferred load.
$\boldsymbol{n}_w$	The unit vector following the wire connecting the crane and the load.
$\boldsymbol{n}_d$	Normal vector defining the plane representing the cargo deck of ship 2.

To understand the ship motions of a vessel at sea, Section 2.3 presents a simplified simulation model of a rigid body ship at sea. The offshore crane placed on top of the main ship is discussed in Section 2.4 and hence the accompanying kinematics and dynamics of the crane are modeled. Section 2.5 presents the process model and measurement models needed to observe the ship-to-ship body motions using multiple sensors placed on the two ships. Finally, a multi-sensor crane assisting system is presented in Section 2.6, which is aimed at increasing both the safety and efficiency of future marine ship-to-ship operations.

2.2 Rigid-Body Kinematics and Mathematical Notation

In this section, the fundamental notation used to describe the geometric relationships between vectors, coordinate systems and bodies are discussed. Both the notation and kinematic formulations are inherited by the one presented in [35] by Thor I. Fossen. However, the notation used in the thesis itself is not necessarily similar to the one presented

in the appended papers. This is due to the fact that the notation and the kinematic modeling technique has evolved during the time of working with this project.

Instead of repeating all the details describing the notation, which anyway can be found in [35], a simple example of a rigid body moving relative to an inertial coordinate system is used to demonstrate the notation used throughout this thesis.

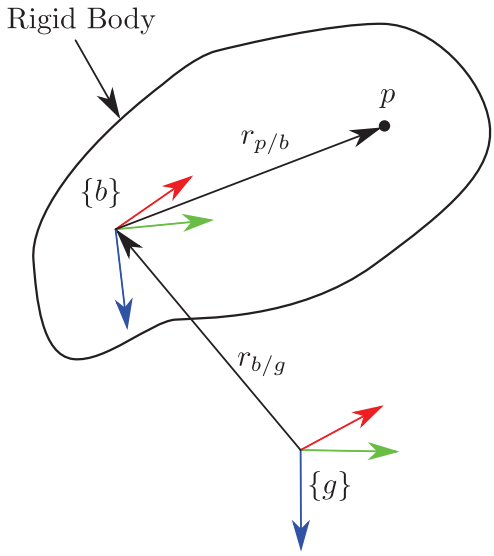

Figure 2.2: Illustration of a point $\boldsymbol{p}$ located on a rigid-body represented by coordinate system $\{b\}$ which is moving relative to the inertial ground given by $\{g\}$.

Figure 2.2 illustrates a point $\boldsymbol{p}$ located on the rigid body $\{b\}$ which can move relative to ground $\{g\}$. The position between the body coordinate $\{b\}$, and the inertial ground coordinate $\{g\}$ are defined using vector $\boldsymbol{r}_{b/g}$, and the orientation of $\{b\}$ relative to $\{g\}$ is given by a rotation matrix $\boldsymbol{R}^g_b$. The subscript of vector $\boldsymbol{r}_{b/g}$ defines the direction of the vector, hence $\boldsymbol{r}_{b/g} = -\boldsymbol{r}_{g/b}$. In addition to the vector subscript describing the direction of the vector, a superscript is used to define which coordinate the vector is given in. If the vector is given in $\{b\}$, the following superscript is used $\boldsymbol{r}^b_{b/g}$, and $\boldsymbol{r}^g_{b/g}$ if it was to be represented in $\{g\}$. To further illustrate the idea, the rotation matrix $\boldsymbol{R}^g_b$ is used to relate the two different vector representations:

$$\boldsymbol{r}^g_{b/g} = \boldsymbol{R}^g_b \boldsymbol{r}^b_{b/g} = \boldsymbol{R}^g_b(-\boldsymbol{r}^b_{g/b}), \qquad \boldsymbol{R}^g_b \in SO(3) \tag{2.1}$$

where $SO(3)$ defines the special orthogonal group which the rotation matrix $\boldsymbol{R}^b_g$ belongs to. Hence the inverse of the rotation matrix is found by simply transposing the rotation matrix as:

$$\boldsymbol{R}^b_g = (\boldsymbol{R}^g_b)^{-1} = (\boldsymbol{R}^g_b)^T. \tag{2.2}$$

The position, velocity and acceleration of point $\boldsymbol{p}$ relative to ground $\{g\}$ are defined by:

$$\boldsymbol{r}^g_{p/g} = \boldsymbol{r}^g_{b/g} + \boldsymbol{R}^g_b \boldsymbol{r}^b_{p/b} \tag{2.3}$$

$$\dot{\boldsymbol{r}}^g_{p/g} = \dot{\boldsymbol{r}}^g_{b/g} + \dot{\boldsymbol{R}}^g_b \boldsymbol{r}^b_{p/b} \tag{2.4}$$

$$\ddot{\boldsymbol{r}}^g_{p/g} = \ddot{\boldsymbol{r}}^g_{b/g} + \ddot{\boldsymbol{R}}^g_b \boldsymbol{r}^b_{p/b} \tag{2.5}$$

which implies that the point $\boldsymbol{p}$ is fixed to the rigid-body $\{b\}$ i.e. $\dot{\boldsymbol{r}}^b_{p/b} = \boldsymbol{0}$. The two time derivatives of the rotation matrix $\boldsymbol{R}^g_b$ are:

$$\dot{\boldsymbol{R}}^g_b = \boldsymbol{R}^g_b \boldsymbol{S}(\boldsymbol{\omega}^b_{b/g}) \tag{2.6}$$

$$\ddot{\boldsymbol{R}}^g_b = \dot{\boldsymbol{R}}^g_b \boldsymbol{S}(\boldsymbol{\omega}^b_{b/g}) + \boldsymbol{R}^g_b \boldsymbol{S}(\dot{\boldsymbol{\omega}}^b_{b/g}) \tag{2.7}$$

$$= \boldsymbol{R}^g_b \boldsymbol{S}(\boldsymbol{\omega}^b_{b/g}) \boldsymbol{S}(\boldsymbol{\omega}^b_{b/g}) + \boldsymbol{R}^g_b \boldsymbol{S}(\dot{\boldsymbol{\omega}}^b_{b/g}) \tag{2.8}$$

where the matrix time derivatives introduce the skew symmetric matrix $\boldsymbol{S}(\cdot)$ and the body fixed velocity $\boldsymbol{\omega}^b_{b/g}$ and acceleration $\dot{\boldsymbol{\omega}}^b_{b/g}$ of body $\{b\}$ relative to ground $\{g\}$ given in the body coordinates $\{b\}$. The skew symmetric matrix is defined as:

$$\boldsymbol{S}(\boldsymbol{\omega}) = \begin{bmatrix} 0 & -\omega_z & \omega_y \\ \omega_z & 0 & -\omega_x \\ -\omega_y & \omega_x & 0 \end{bmatrix}, \quad \boldsymbol{\omega} = \begin{bmatrix} \omega_x \\ \omega_y \\ \omega_z \end{bmatrix} \tag{2.9}$$

where ω_x, ω_y and ω_z represent the body fixed velocity of the rigid body given in the rigid body's coordinate system around the x-, y-, and z-axis respectively.

It is also worth mentioning that almost all the vectors and variables throughout the whole thesis are time-dependent. To save space and avoiding equations to span more than one line it has been chosen to not write the time dependency for each variable i.e.

$$\boldsymbol{x}(t) \rightarrow \boldsymbol{x}. \tag{2.10}$$

However, where the vector is not time dependent it has been clarified in the text that the vector or parameter is non-time dependent and that the corresponding time derivative is zero.

2.3 Hydrodynamic Ship Disturbance Model

To understand the type of forces, and hence also the motions which an offshore ship is experiencing during offshore operations, one could consider using logged data from a real vessel. However, in this section a simplified simulation model of a rigid ship is used to simulate the ship body motions as a result of stochastic wave forces generated using the methods and techniques presented in [35]. The simulation model used to simulate the ship motions are given by:

$$\dot{\boldsymbol{\eta}} = \boldsymbol{J}(\boldsymbol{\eta})\boldsymbol{v} \tag{2.11}$$

$$[\boldsymbol{M}_{RB} + \boldsymbol{M}_A]\,\dot{\boldsymbol{v}} + \boldsymbol{D}\boldsymbol{v} + \boldsymbol{G}\boldsymbol{\eta} = \boldsymbol{\tau}_{DP} + \boldsymbol{\tau}_{wave} \tag{2.12}$$

where the ship attitude is defined by $\boldsymbol{\eta}$, the ship velocity is $\boldsymbol{v}$ and hence also the acceleration is given by $\dot{\boldsymbol{v}}$. The position, velocity and acceleration are described in more details using:

$$\boldsymbol{\eta} = \begin{bmatrix} \boldsymbol{r}^n_{b/n} \\ \boldsymbol{\Theta}_{nb} \end{bmatrix}, \quad \boldsymbol{v} = \begin{bmatrix} \dot{\boldsymbol{r}}^n_{b/n} \\ \boldsymbol{\omega}^b_{b/n} \end{bmatrix}, \quad \dot{\boldsymbol{v}} = \begin{bmatrix} \ddot{\boldsymbol{r}}^n_{b/n} \\ \dot{\boldsymbol{\omega}}^b_{b/n} \end{bmatrix} \tag{2.13}$$

where $\boldsymbol{r}^n_{b/n} = [x, y, z]^T$ is the ship body $\{b\}$ position relative to the inertial coordinate system $\{n\}$, and $\boldsymbol{\Theta}_{nb} = [\phi, \theta, \psi]^T$ are the Euler angles describing the body attitude relative to the inertial coordinate. The model matrices are inherited from the Marine Systems Simulator (MSS) which is documented in [36], [37] and [38]. The model matrices describing the rigid ship body mass $\boldsymbol{M}_{RB}$, the added hydrodynamic mass $\boldsymbol{M}_A$, the viscous damping forces $\boldsymbol{D}$, and finally the restoring forces $\boldsymbol{G}$ represent a supply vessel which is found in the MSS toolbox available at `http://www.marinecontrol.org/`. The transforming Jacobian $\boldsymbol{J}(\boldsymbol{\eta})$ found in Eq. (2.11) relates the two ship velocity representations $\dot{\boldsymbol{\eta}}$ and $\boldsymbol{v}$ as:

$$\boldsymbol{J}(\boldsymbol{\eta}) = \begin{bmatrix} \boldsymbol{I} & \boldsymbol{0} \\ \boldsymbol{0} & \boldsymbol{T}_\Theta(\boldsymbol{\Theta}_{nb}) \end{bmatrix} \tag{2.14}$$

where the transformation matrix $\boldsymbol{T}_\Theta(\boldsymbol{\Theta}_{nb})$ is defined by:

$$\boldsymbol{T}_\Theta(\boldsymbol{\Theta}_{nb}) = \frac{1}{\cos(\theta)} \begin{bmatrix} \cos(\theta) & \sin(\phi)\sin(\theta) & \cos(\phi)\sin(\theta) \\ 0 & \cos(\phi)\cos(\theta) & -\sin(\phi)\cos(\theta) \\ 0 & \sin(\phi) & \cos(\phi) \end{bmatrix}, \quad \cos(\theta) \neq 0 \tag{2.15}$$

given that rotation matrix $\boldsymbol{R}^n_b(\boldsymbol{\Theta_{nb}})$ describing the ship attitude is following the ZYX-angle sequence as:

$$\boldsymbol{R}^n_b(\boldsymbol{\Theta_{nb}}) = \boldsymbol{R}_z(\psi)\boldsymbol{R}_y(\theta)\boldsymbol{R}_x(\phi) \tag{2.16}$$

where $\boldsymbol{R}_x$, $\boldsymbol{R}_y$ and $\boldsymbol{R}_z$ are the well known rotation matrices used to rotate about the x-, y-, and z-axis respectively. If the angle sequence differs from the ZYX-angle sequence described here, the transforming Jacobian must use another $\boldsymbol{T}_\Theta(\boldsymbol{\Theta}_{nb})$ which reflects the angle sequence used to describe the rotation matrix $\boldsymbol{R}^n_b(\boldsymbol{\Theta_{nb}})$.

2.3.1 Stochastic Wave Forces

In Eq. (2.12), there are two generalized force vectors representing the dynamic positioning system $\boldsymbol{\tau}_{DP}$, and the wave disturbance forces $\boldsymbol{\tau}_{\text{wave}}$. In reality, there exist plenty of other disturbances such as ocean currents and wind forces only to mention some. However, it is desired to stick with the simplified model, since the most important task of the simulation model is to generate suitable stochastic ship motions in all six degrees of freedom. The stochastic wave force for each degree of freedom is modeled as:

$$\tau^{\text{dof}}_{\text{wave}} \approx K^{\text{dof}} h(s) w^{\text{dof}}(s), \quad \text{dof} \in [1 \cdots 6] \tag{2.17}$$

where $h(s)$ and $w^{\text{dof}}(s)$ are given in the Laplace domain, and $\tau^{\text{dof}}_{\text{wave}}$ is given in the time domain. From a pure mathematical point of view, combining both the time and Laplace domain in a single equation is wrong, but is only written in this way to illustrate that the stochastic wave forces are generated using a transfer function which has its input driven by a zero-mean white noise process $w^{\text{dof}}(s)$. The transfer function used to simulate the wave force magnitude is given by:

$$h(s) = \frac{2\lambda\omega_0\sigma s}{s^2 + 2\lambda\omega_0 s + \omega_o^2} \tag{2.18}$$

where ω_0 describes the wave peak frequency, λ is the wave damping ratio, and σ defines the wave intensity. The transfer function is unchanged for each degree of freedom, whereas the zero-mean white noise processes $w^{\text{dof}}(s)$ and the tunable gain K^{dof} are individual for each degree of freedom. Since the goal of the transfer function is to relate the stochastic wave forces to a specific wave spectrum $S(\omega)$, the transfer function coefficients are derived from solving the following minimization problem:

$$\underset{\lambda,\omega_0,\sigma}{\text{minimize}} \quad \left[|h(j\omega)|^2 - S(\omega)\right]^T \left[|h(j\omega)|^2 - S(\omega)\right] \tag{2.19}$$

where the resulting magnitude of the transfer function $|h(j\omega)|^2$ can be compared with the chosen wave spectrum $S(\omega)$ as illustrated in Figure. 2.3.

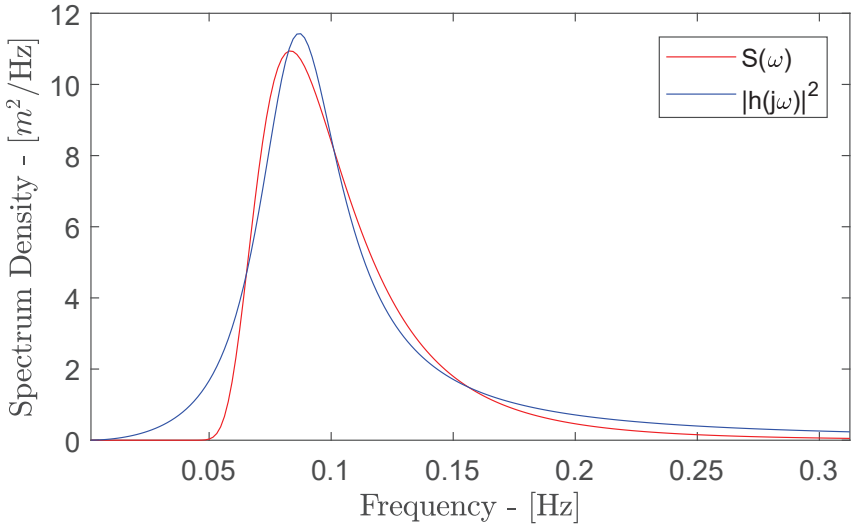

Figure 2.3: Linearized wave energy spectrum as illustrated in Paper E which compares the Pierson-Moskowitz wave spectrum against the linear appropriation.

The magnitude of the linear transfer function $|h(j\omega)|^2$ represents an acceptable approximation of the wave spectrum, which in our example was represented using the Pierson-Moskowitz wave spectrum [39] with a significant wave height $H_s = 8m$ and a typical wave period of $T_p = 12.0s$. Other wave spectra such as the JONSWAP spectrum [40] could also be used in the same manner without the need for another transfer function, only updating the corresponding coefficients.

2.3.2 Simplified DP-System

The stochastic wave forces described in the previous section will cause the ship do drift away in all three directions representing the surge, sway and yaw directions i.e. x, y, and ψ. In most ship-to-ship scenarios, the ships are usually controlled by some kind of Dynamic Positioning system, hereby named DP-system. This system is used to keep the surge, sway and yaw motions to desired values, hence meaning that the DP-control

problem is defined by:

$$\lim_{t\to\infty} \boldsymbol{e}_{DP} = \begin{bmatrix} x_d - x \\ y_d - y \\ \psi_d - \psi \end{bmatrix} \to \mathbf{0} \tag{2.20}$$

where $\boldsymbol{e}_{DP}$ is the DP error signal to be minimized using a suitable control system controlling the ship thrusters and rudders. Both the industry and the academia have been researching this topic for many years and a lot of proposed methods to solve this problem is presented in [41], [42] and [43] to only mention some. However, as the motivation of this simulation model is to have a simple simulation model capable of being deployed onto a real-time target, a simplified controller representing the DP-System is formed by a PD-controller:

$$\boldsymbol{\tau}_{DP} = \boldsymbol{K}_p \boldsymbol{e}_{DP} + \boldsymbol{K}_d \dot{\boldsymbol{e}}_{DP} \tag{2.21}$$

where each of the controller gains are found from pole placement where the system dynamics were identified through a step response and hence modeled using a 1^{st} order transfer function for the surge, sway and yaw directions. The controller gains $\boldsymbol{K}_p$ and $\boldsymbol{K}_d$ were then found from comparing the coefficients of the characteristic polynomial of the closed-loop system $p(s) = f(\tau, K_{SS}, K_p, K_d)$ and the desired characteristic polynomial $p_d(s) = (s-d)^2$, where d is the desired pole placement. The time constant τ and the steady state gain K_{SS} are found from the previously mentioned step response.

2.3.3 Simulink Implementation

Simulink was used to realize the time domain simulation and hence the resulting Simulink block diagram is depicted in 2.4.

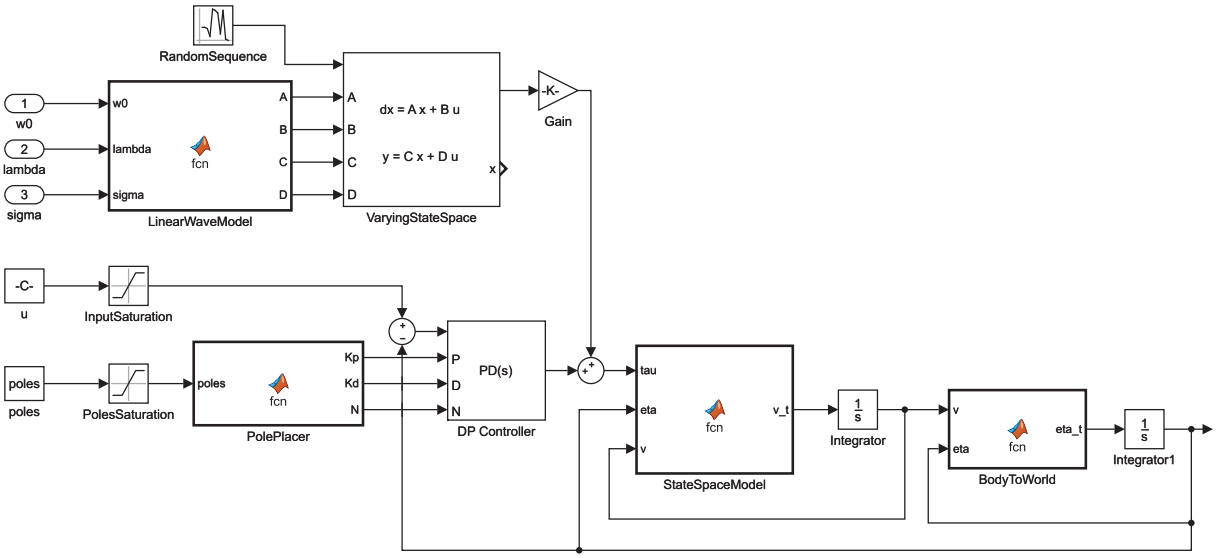

Figure 2.4: Implementation of the ship motion simulation model which also is deployed in the Norwegian Motion Laboratory with the use of Beckhoff's TwinCAT Simulink code generation tool.

The goal of the simulation is to generate a suitable disturbance motion which can be used to move the two Stewart platforms in the motion laboratory. To accomplish this, a real-time implementation of the block diagram has been used to deploy the simulation model to the embedded PC (Beckhoff CX2040). The real-time code generation is carried out using the Beckhoff's TwinCAT Simulink coder functionality which compiles the Simulink model into a TcCOM object (C++ based). This TcCOM object is downloaded and executed on the embedded PC in real-time, where the exported TcCOM object is depicted in Figure 2.5. The two simulated outputs `em8000.control` and `em1500.control` are used to move the two Stewart platforms with stochastic motions simulating two supply ships laying alongside each other at sea. The linearized wave spectrum parameters are calculated by the HMI and used to define the TcCOM inputs `w0`, `lambda` and `sigma`.

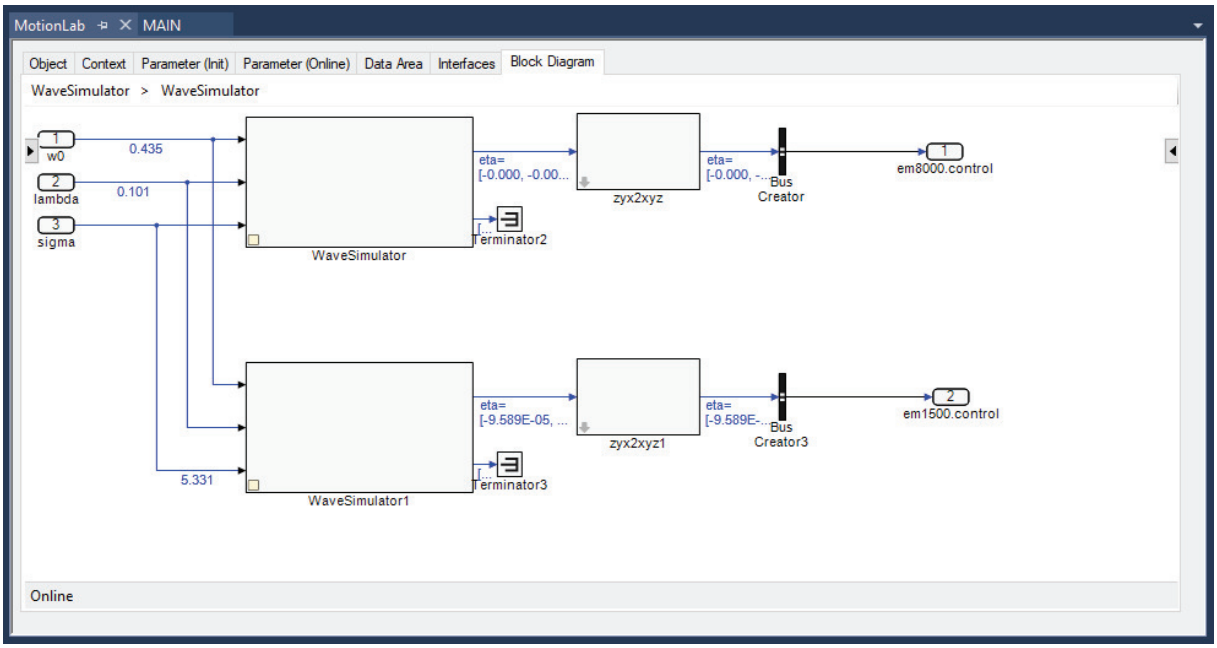

Figure 2.5: The resulting TcCOM block diagram in Microsoft Visual Studio after deployment to the CX2040 where the Simulink model depicted in Figure 2.4 has been reused to simulate the stochastic ship motions controlling the two Stewart platforms in real-time.

2.4 Crane Modeling

This section will present the general equations describing the forward and the inverse kinematics of the offshore crane depicted in Figure 2.6. Since no physical parameters of the crane are considered throughout this chapter, only the methods needed to form the required equations will be discussed to gain a fundamental understanding of the crane kinematics. A short discussion on the crane dynamics and the accompanying control system will be elaborated briefly at the end of this section, but the closed loop dynamics of the crane is later considered as a black box and hence not used in the design of the multi-sensor crane operator assistant presented in Section 2.6.

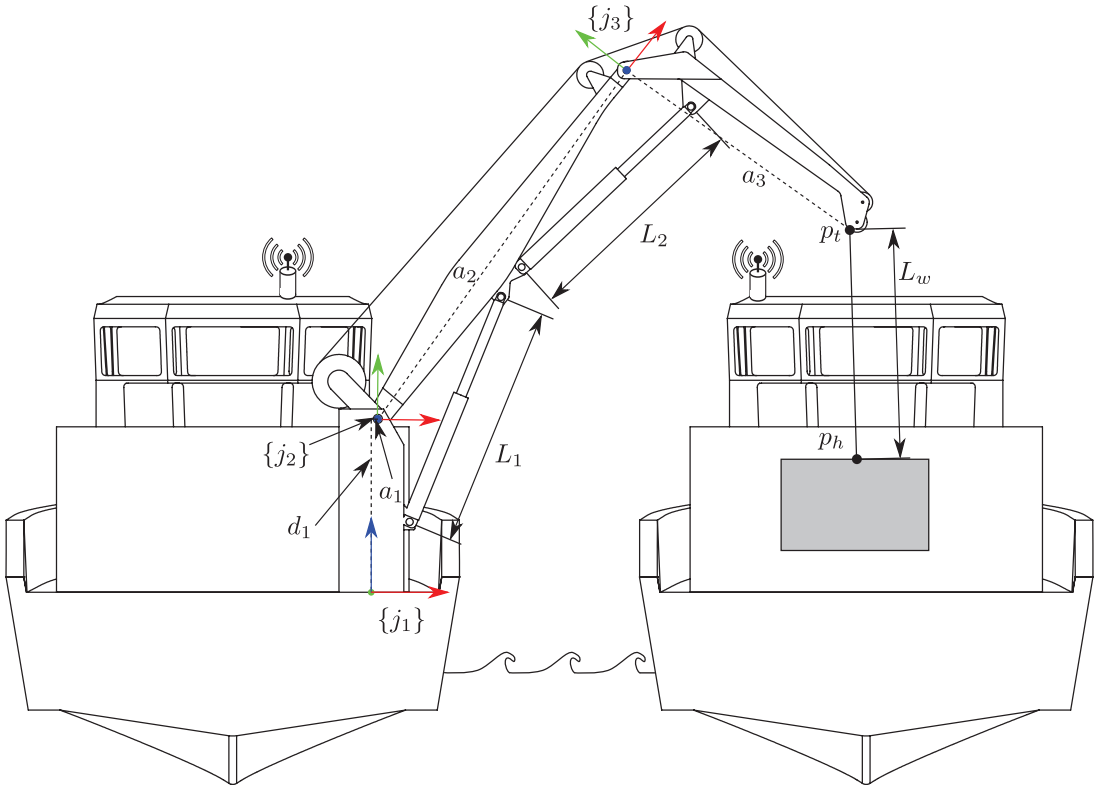

Figure 2.6: Crane kinematics illustrating the accompanying DH-parameters and joint coordinate systems $\{j_i\}$.

2.4.1 Forward Kinematics

Figure 2.6 illustrates the coordinate systems and the lengths of the rigid links forming the kinematic structure of the offshore crane. Three new coordinate systems $\{j_1\}$, $\{j_2\}$ and $\{j_3\}$ are introduced in addition to the one presented in Figure 2.1. These coordinate systems represent the revolute joints of the crane, where the positive rotation angle θ_i of each revolute joint i is defined to be around the z-axis (blue). It should also be noted that the coordinate system $\{c\}$ and $\{j_1\}$ are assumed to be equal to each other, hence the respective homogeneous transformation is $\boldsymbol{H}_{j_1}^{c} = \boldsymbol{I}$.

The forward kinematics describes the position, velocity and acceleration of the crane tip $\boldsymbol{p}_t$ relative to crane base coordinate system ($\{c\} = \{j_1\}$). Usually the forward kinematics is formulated using the Denavit-Hartenberg [44, 45] convention also known as DH-table of the rigid-body link mechanism. The DH-table describes the relative homogeneous transformation from one joint $i-1$ to the next joint i using the following homogeneous transformation:

$$\boldsymbol{H}_i^{i-1}(\theta_i, d_i, a_i, \alpha_i) = \boldsymbol{R}_z(\theta_i)\boldsymbol{T}_z(d_i)\boldsymbol{T}_x(a_i)\boldsymbol{R}_x(\alpha_i) \tag{2.22}$$

where the accompanying DH-table defining θ_i, d_i, a_i, and α_i are given in Table 2.2.

Table 2.2: DH-table for the crane seen in Figure 2.6.

Transformation	θ_i	d_i	a_i	α_i
$\boldsymbol{H}_{j_2}^{j_1}$	$\theta_1 = \theta_{\text{slew}}$	d_1	a_1	90°
$\boldsymbol{H}_{j_3}^{j_2}$	$\theta_2 = f_{\text{C1}}(L_1)$	0	a_2	0°
$\boldsymbol{H}_{t}^{j_3}$	$\theta_3 = f_{\text{C2}}(L_2)$	0	a_3	0°

The joint angles θ_1, θ_2 and θ_3 describe the revolute joint space $\boldsymbol{\theta} = [\theta_1, \theta_2, \theta_3]^T$, and are related to the controllable joints, either linearly as seen for the slew angle θ_{slew}, or non-linearly for θ_2 and θ_3 which are a function of the cylinder stroke lengths L_1 and L_2 respectively. Using the DH-table, the homogeneous transformation from the crane base $\{c\}$ to the crane tip $\{t\}$ is derived:

$$\boldsymbol{H}_t^c = \boldsymbol{H}_{j_1}^c \boldsymbol{H}_{j_2}^{j_1} \boldsymbol{H}_{j_3}^{j_2} \boldsymbol{H}_{j_t}^{j_3} = \begin{bmatrix} \boldsymbol{R}_t^c & \boldsymbol{r}_{t/c}^c \\ \boldsymbol{0} & 1 \end{bmatrix} \tag{2.23}$$

where the crane tip position is used to define the forward kinematics of the crane i.e.

$$\boldsymbol{r}_{t/c}^c = \boldsymbol{f}_{\text{FK}}(\boldsymbol{q}) \tag{2.24}$$

where

$$\boldsymbol{q} = [\theta_{\text{slew}}, L_1, L_2]^T = \boldsymbol{f}(\boldsymbol{\theta}) \tag{2.25}$$

is defined as the controllable joint space which is non-linearly dependent on the revolute joint space $\boldsymbol{\theta}$. The forward kinematics in Eq. (2.24) is used to derive both the velocity and acceleration of the crane tip:

$$\dot{\boldsymbol{r}}_{t/c}^c = \boldsymbol{J}_{\boldsymbol{q}}(\boldsymbol{q})\dot{\boldsymbol{q}} \tag{2.26}$$

$$\ddot{\boldsymbol{r}}_{t/c}^c = \dot{\boldsymbol{J}}_{\boldsymbol{q}}(\boldsymbol{q})\dot{\boldsymbol{q}} + \boldsymbol{J}_{\boldsymbol{q}}(\boldsymbol{q})\ddot{\boldsymbol{q}} \tag{2.27}$$

where the Jacobian matrix $\boldsymbol{J}_{\boldsymbol{q}}(\boldsymbol{q})$ is:

$$\boldsymbol{J}_{\boldsymbol{q}}(\boldsymbol{q}) = \frac{\partial \boldsymbol{f}_{\text{FK}}}{\partial \boldsymbol{q}} \tag{2.28}$$

where the partial derivatives of the forward kinematics are used to form the Jacobian matrix. The forward kinematic study is therefore fundamental both to understand the forward kinematics of the crane, but also to form the Jacobian matrix which will be used again in the next section when deriving the inverse kinematics.

2.4.2 Inverse Kinematics

Knowing the forward kinematics presented in the previous section, the inverse kinematics is needed to calculate $\boldsymbol{q}$ as a function of the crane tip position $\boldsymbol{r}_{t/c}^c$ i.e.

$$\boldsymbol{q} = \boldsymbol{f}_{\text{IK}}(\boldsymbol{r}_{t/c}^c). \tag{2.29}$$

where the inverse kinematics usually are solved analytically or numerically [46]. The controllable joint velocity $\dot{\boldsymbol{q}}$ and acceleration $\ddot{\boldsymbol{q}}$ are found from rearranging Eq. (2.26) and Eq. (2.27) into:

$$\dot{\boldsymbol{q}} = \boldsymbol{J}_{\boldsymbol{q}}^{-1}(\boldsymbol{q})\dot{\boldsymbol{r}}_{t/c}^{c} \tag{2.30}$$

$$\ddot{\boldsymbol{q}} = \boldsymbol{J}_{\boldsymbol{q}}^{-1}(\boldsymbol{q})\left(\ddot{\boldsymbol{r}}_{t/c}^{c} - \dot{\boldsymbol{J}}_{\boldsymbol{q}}(\boldsymbol{q})\dot{\boldsymbol{q}}\right) \tag{2.31}$$

which represent the velocity and acceleration of the controllable joints.

The inverse kinematics is fundamental to map the desired crane tip motion to equivalent values for the controllable joint space, which is then used as input to the crane control system to move the crane in the desired motion, also known as tool point control in robotics.

2.4.3 General Dynamics and Control

Since the crane control system and hence also the dynamics of the crane are assumed to be more or less unknown it is only presented using generalized equations to briefly have a key understating of the crane dynamics and the accompanying control system. The crane dynamics can be described using the generalized coordinates $\boldsymbol{q}$ which were mentioned in the two previous sections, which again leads to the generalized equation of motion:

$$\boldsymbol{M}(\boldsymbol{q})\ddot{\boldsymbol{q}} + \boldsymbol{C}(\boldsymbol{q},\dot{\boldsymbol{q}})\dot{\boldsymbol{q}} + \boldsymbol{g}(\boldsymbol{q}) = \boldsymbol{\tau_q} + \boldsymbol{\tau_d}, \quad \boldsymbol{\tau_q} = [\tau_{\text{slew}}, f_{\text{C1}}, f_{\text{C2}}]^T \tag{2.32}$$

where $\boldsymbol{M}(\boldsymbol{q})$ is the crane inertia matrix, $\boldsymbol{C}(\boldsymbol{q},\dot{\boldsymbol{q}})$ is the Coriolis-centrifugal matrix, $\boldsymbol{q}(\boldsymbol{q})$ is the gravity vector, $\boldsymbol{\tau_q}$ is the generalized control force input used to operate the crane, and $\boldsymbol{\tau_d}$ is the generalized disturbances acting on the crane. However, since most industrial cranes are highly non-linear due to the closed loop kinematic chains introduced by the hydraulic cylinders and the hydraulic actuations system itself, the control problem of operating the offshore crane with high dynamic performance is in general classified as a challenging task. In this study the crane control system is defined to be a general control system using a cascaded feedback and a feedforward as illustrated in Figure 2.7.

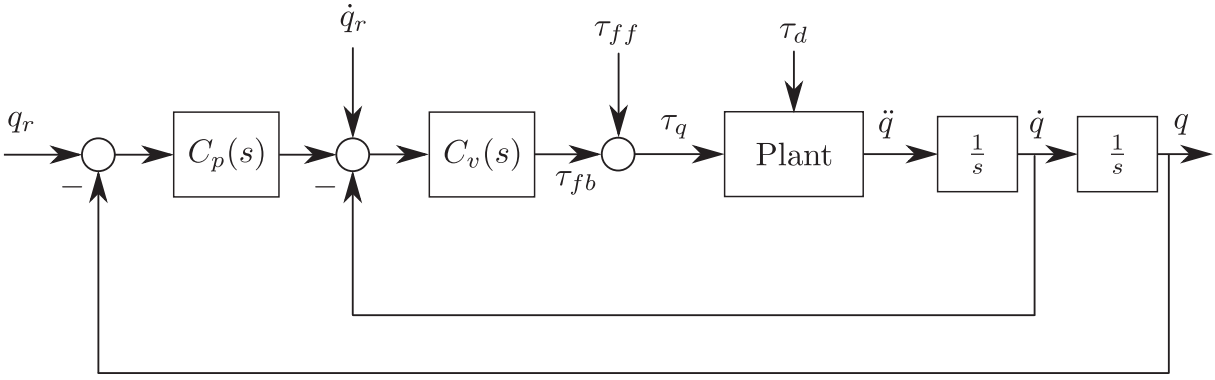

Figure 2.7: General control structure for an offshore crane with a cascaded feedback control system and the added model-based feedforward control input.

The two feedback controllers $C_v(s)$ and $C_p(s)$ used to control the velocity and position are usually based on linear control theory where a linear system dynamics are assumed

due to the feedforward torque $\boldsymbol{\tau}_{ff}$ which is usually based on the crane model. The work presented later will only focus on the input control reference generation for the control system illustrated here, which is assumed to be already fitted with the crane i.e. the closed-loop dynamics of the crane is seen as a black box system where only the kinematics are considered for correct crane reference input $\boldsymbol{q}_r$ and $\dot{\boldsymbol{q}}_r$.

2.5 Ship-to-Ship State Estimation

This section will discuss the kinematic modeling which forms the fundamental understanding of the relative body motions between two ships situated at sea. To move the crane and the load in a suitable motion for increased safety and efficiency, the observation of this relative motions is considered a crucial task. The content of this section can be seen as a result of the research carried out in the previously published Papers C, D and E.

2.5.1 Kinematics

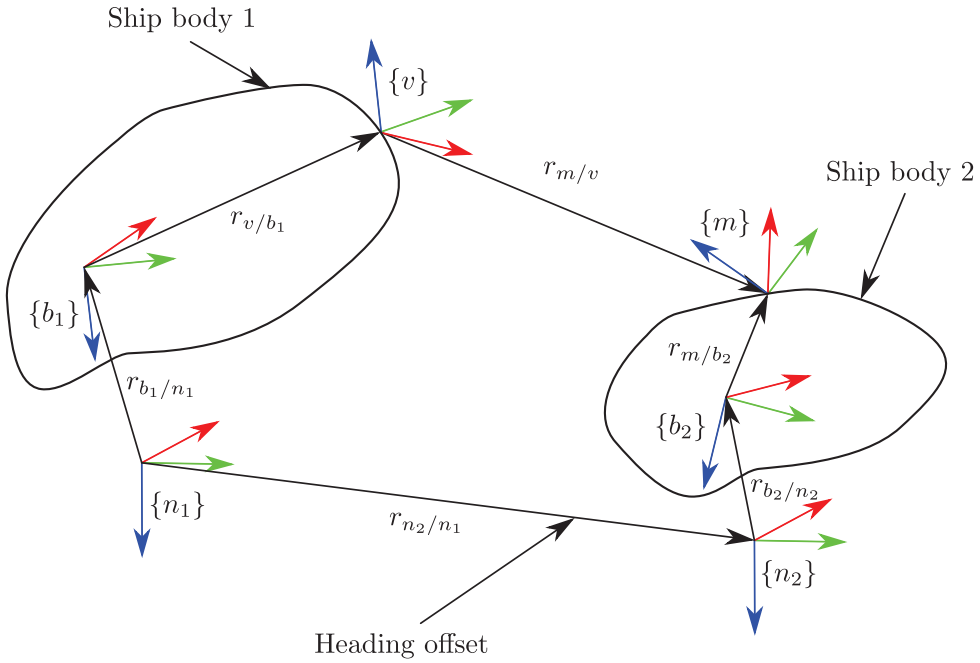

Figure 2.8: Ship-to-ship kinematics used to form the fundamental equations for both the process and the measurement models.

The two ships are modeled as two independent rigid bodies without influencing each other. Both ship bodies $\{b_1\}$ and $\{b_2\}$ have been modeled to operate around their respective heading coordinates $\{n_1\}$ and $\{n_2\}$, e.g. they move with zero mean motion in the surge, sway, heave, roll pitch and yaw directions relative to their respective heading coordinates. The heading coordinate z-axis (blue) is always pointing downwards along the gravitational direction. The visual sensor placed on the main ship (Ship body 1) is supposed to measure the absolute pose between the visual sensor coordinate $\{v\}$ and the marker $\{m\}$ placed

onto the secondary ship body. Both the visual sensor and the marker is assumed to be fixed to each of the ships i.e.

$$\frac{d}{dt}\boldsymbol{r}_{v/b_1}^{b_1} = \frac{d}{dt}\boldsymbol{\Theta}_{b_1 v} = \frac{d}{dt}\boldsymbol{r}_{m/b_2}^{b_2} = \frac{d}{dt}\boldsymbol{\Theta}_{b_2 m} = \mathbf{0}. \tag{2.33}$$

Previously in Figure 2.1, there were indicated two MRU sensors mounted onto each of the two ships, but in this representation, they are not modeled explicitly since it is assumed that the internal MRU software of each MRU is calibrated to measure the ship body movement instead of the MRU body movement i.e.

$$\{b_1\} = \{m_1\} \quad \text{and} \quad \{b_2\} = \{m_2\}. \tag{2.34}$$

2.5.2 Process Model

The relative ship pose has to be estimated in real-time for successful operation of the offshore crane in ship-to-ship operations. As for most common real-time estimation tasks, the use of estimation algorithms such as the Kalman filters, (KF), the Extended Kalman Filter (EKF), and the Particle Filter (PF), requires both the process and the measurements to be modeled. These models relate the process and the measurements to a common state vector $\boldsymbol{x}_s$, which is to be estimated by the algorithm. The state vector used to describe the ship-to-ship estimation problem is:

$$\boldsymbol{x}_s = \begin{bmatrix} \boldsymbol{\eta}_1 \\ \boldsymbol{v}_1 \\ \boldsymbol{\eta}_2 \\ \boldsymbol{v}_2 \\ \boldsymbol{o} \end{bmatrix} \tag{2.35}$$

where $\boldsymbol{\eta}_1$ and $\boldsymbol{\eta}_2$ parameterize the positions of both the ships, $\boldsymbol{v}_1$ and $\boldsymbol{v}_2$ define the two ship velocities and finally $\boldsymbol{o}$ represents the heading offset. The heading offset is assumed to be a slowly varying offset between the two heading coordinates $\{n_1\}$ and $\{n_2\}$ i.e. the heading offset is parameterized $\boldsymbol{o} = [x_o, y_o, \Psi_o]^T$, and is related to Figure 2.8 using:

$$\boldsymbol{r}_{n_2/n_1}^{n_1} = \begin{bmatrix} x_o & y_o & 0 \end{bmatrix}^T \quad \text{and} \quad \boldsymbol{R}_{n_2}^{n_1} = \boldsymbol{R}_z(\Psi_o). \tag{2.36}$$

The remaining parts of the state vector $\boldsymbol{x}_s$ are directly related to the ship-to-ship kinematics seen in Figure 2.8 according to:

$$\boldsymbol{\eta_1} = \begin{bmatrix} \boldsymbol{r}_{b_1/n_1}^{n_1} \\ \boldsymbol{\Theta}_{n_1 b_1} \end{bmatrix}, \quad \boldsymbol{v}_1 = \begin{bmatrix} \dot{\boldsymbol{r}}_{b_1/n_1}^{n_1} \\ \boldsymbol{\omega}_{b_1/n_1}^{b_1} \end{bmatrix}, \tag{2.37}$$

$$\tag{2.38}$$

$$\boldsymbol{\eta_2} = \begin{bmatrix} \boldsymbol{r}_{b_2/n_2}^{n_2} \\ \boldsymbol{\Theta}_{n_2 b_2} \end{bmatrix}, \quad \boldsymbol{v}_2 = \begin{bmatrix} \dot{\boldsymbol{r}}_{b_2/n_2}^{n_2} \\ \boldsymbol{\omega}_{b_2/n_2}^{b_2} \end{bmatrix}. \tag{2.39}$$

By recalling the ship kinematics defined in Section 2.3, the time-continuous process model of our estimation problem is:

$$\dot{\boldsymbol{x}}_s = \underbrace{\begin{bmatrix} \boldsymbol{J}(\boldsymbol{\eta}_1)\boldsymbol{v}_1 \\ \boldsymbol{0} \\ \boldsymbol{J}(\boldsymbol{\eta}_2)\boldsymbol{v}_2 \\ \boldsymbol{0} \\ \boldsymbol{0} \end{bmatrix}}_{\boldsymbol{f}(\boldsymbol{x}_s)} + \boldsymbol{w} \tag{2.40}$$

where the ship body velocity Jacobians $\boldsymbol{J}(\boldsymbol{\eta}_1)$ and $\boldsymbol{J}(\boldsymbol{\eta}_2)$ are defined by Eq. (2.14), and $\boldsymbol{w}$ is the process noise which is assumed to be additive. It should also be mentioned that the ship model presented in Section 2.3 is not included in the process model i.e. $\dot{\boldsymbol{v}}_1$ and $\dot{\boldsymbol{v}}_2$ are modeled as zero. Adding the ship models would most likely increase the estimation performance further, but on the other hand also the specific models matrices of each of the ships had to be known.

2.5.3 Measurement Models

The measurements models relate the measurements $\boldsymbol{z}$ to the state vector $\boldsymbol{x}_s$ e.g. $\boldsymbol{z} = \boldsymbol{h}(\boldsymbol{x}_s)$, where $\boldsymbol{h}(\boldsymbol{x}_s)$ is the measurement model. It is assumed that a suitable low latency wireless connection is used to transfer sensor data between the two ships in real-time e.g. as in Paper A. Since the two MRUs were calibrated to measure the ship body motions directly, the two MRU measurement models are linearly dependent to the state vector as:

$$\boldsymbol{z}_{\text{mru}_1} = \boldsymbol{h}_{\text{mru}_1}(\boldsymbol{x}_s) = \begin{bmatrix} \boldsymbol{\eta}_1 \\ \boldsymbol{v}_1 \end{bmatrix} + \boldsymbol{v}_{\text{mru}_1} \quad \text{and} \quad \boldsymbol{z}_{\text{mru}_2} = \boldsymbol{h}_{\text{mru}_2}(\boldsymbol{x}_s) = \begin{bmatrix} \boldsymbol{\eta}_2 \\ \boldsymbol{v}_2 \end{bmatrix} + \boldsymbol{v}_{\text{mru}_2} \tag{2.41}$$

where $\boldsymbol{v}_{\text{mru}_1}$ and $\boldsymbol{v}_{\text{mru}_2}$ are the sensor noise of the two MRUs. To estimate the heading offset parameters $\boldsymbol{o}$, a high precision Global Navigation Satellite System (GNSS) could be applied to measure both the heading and the position of both the two heading coordinates directly.

A high precision GNSS implies that recent technologies within Global Positioning System (GPS) is applied to achieve higher precision than standard GPS solutions. Such technology exists, and the two main methods are the Real Time Kinematics (RTK) and the Precise Point Positioning (PPP). The PPP solution does not require a fixed base GPS station for calibration purpose and may be the most promising technology when applied to ship-to-ship state estimation. PPP has been experimentally investigated in [47] and the results state that the horizontal positioning error is less than $10cm$. In addition, [48] states that PPP will improve traditional GPS technology with a factor of 100. The reason that this technology is not standard in all GPS receivers today is that the PPP algorithm requires the satellite correction data to be transmitted together with the standard satellite data packet, meaning that you need an external data link to fetch the correction data on regular basis. It is therefore believed that future GNSS solutions will be accurate enough for this specific application, and hence be included using the following measurement model:

$$\boldsymbol{z}_{\text{gnss}} = \boldsymbol{z}_{\text{gnss}_2} - \boldsymbol{z}_{\text{gnss}_1} = \boldsymbol{h}_{\text{gnss}}(\boldsymbol{x}_s) = \boldsymbol{o} + \boldsymbol{v}_{\text{gnss}} \tag{2.42}$$

which again is found to be linearly dependent to the state vector $\boldsymbol{x}_s$. In offshore applications in general, redundancy is of high importance. Redundancy could have been achieved by including more GNSS systems, or by adding a visual sensor capable of tracking the relative motions between the two ship bodies directly using a camera system as presented in Paper C or by using a laser tracker as the one presented in Paper D. This measurement is then supposed to measure the pose of the marker $\{m\}$ relative to the visual sensor $\{v\}$, hence given as the following measurement model:

$$\boldsymbol{z}_{\text{visual}} = \boldsymbol{h}_{\text{visual}}(\boldsymbol{x}_s) = \begin{bmatrix} \boldsymbol{r}^v_{m/v} \\ \boldsymbol{q}^v_m \end{bmatrix} + \boldsymbol{v}_{\text{visual}} \tag{2.43}$$

where the position of the marker is given by:

$$\boldsymbol{r}^v_{m/v} = (\boldsymbol{R}^{n_1}_{b_1}\boldsymbol{R}^{b_1}_v)^T(\boldsymbol{r}^{n_1}_{m/n_1} - \boldsymbol{r}^{n_1}_{v/n_1}) \tag{2.44}$$

and the accompanying orientation of the marker is:

$$\boldsymbol{q}^v_m = \boldsymbol{f}(\boldsymbol{R}^v_m) \tag{2.45}$$

where $\boldsymbol{q}^v_m$ is the unit quaternion which is a function of the corresponding rotation matrix:

$$\boldsymbol{R}^v_m = (\boldsymbol{R}^{n_1}_{b_1}\boldsymbol{R}^{b_1}_v)^T(\boldsymbol{R}_z(\Psi_o)\boldsymbol{R}^{n_2}_{b_2}\boldsymbol{R}^{b_2}_m). \tag{2.46}$$

The measurement model for using the visual sensor is by no means linearly dependent to the state vector $\boldsymbol{x}_s$. A linearization of the measurement model is therefore needed for implementation later using the EKF. This is also true for the process model, and hence this linearization step will be discussed briefly in the next section where the algorithmic implementation is presented.

2.5.4 EKF Implementation

For the algorithmic implementation of the time continuous process model and the measurement models presented in the previous two sections, a time-discrete process model is required and hence derived as:

$$\boldsymbol{x}_k = \underbrace{\boldsymbol{x}_{k-1} + \boldsymbol{f}(\boldsymbol{x}_{k-1})T_s}_{\boldsymbol{f}_k(\boldsymbol{x}_{k-1}, T_s)} + \boldsymbol{w}_k \tag{2.47}$$

where the process model is discretized using the first order backward Euler approximation. Furthermore, the process and the measurement models are linearized using:

$$\boldsymbol{F}_k = \left.\frac{\partial \boldsymbol{f}_k}{\partial \boldsymbol{x}}\right|_{\hat{\boldsymbol{x}}_{k-1|k-1}} \qquad \boldsymbol{H}_{s,k} = \left.\frac{\partial \boldsymbol{h}_s}{\partial \boldsymbol{x}}\right|_{\hat{\boldsymbol{x}}_{k|k-1}} \tag{2.48}$$

where k is the k'th time step, $\boldsymbol{h}_s$ is the measurement model of sensor s, $\hat{\boldsymbol{x}}_{k-1|k-1}$ represents the previous state estimate, and $\hat{\boldsymbol{x}}_{k|k-1}$ is the current state estimate prediction. By applying the standard Extended Kalman Filter (EKF) as presented in Algorithm 1, the process can be estimated in real-time.

Algorithm 1 Extended Kalman Filter Implementation

$k \leftarrow 1$
$\hat{\boldsymbol{x}}_{k-1|k-1} \leftarrow \boldsymbol{x}_0$
$\boldsymbol{P}_{k-1|k-1} \leftarrow \boldsymbol{P}_0$
loop
  // Predict state and state covariance
  $\hat{\boldsymbol{x}}_{k|k-1} \leftarrow \boldsymbol{f}_k(\hat{\boldsymbol{x}}_{k-1|k-1}, T_s)$
  $\boldsymbol{P}_{k|k-1} \leftarrow \boldsymbol{F}_k \boldsymbol{P}_{k-1|k-1} \boldsymbol{F}_k^T + \boldsymbol{Q}_k$

  // Form $\boldsymbol{H}_k, \boldsymbol{R}_k$ and $\boldsymbol{y}_k$ given available measurements
  $\boldsymbol{H}_k \leftarrow \begin{bmatrix} \boldsymbol{H}_{\text{mru}_1,k} \\ \boldsymbol{H}_{\text{mru}_2,k} \end{bmatrix} \quad \boldsymbol{R}_k \leftarrow \begin{bmatrix} \boldsymbol{R}_{\text{mru}_1} & \boldsymbol{0} \\ \boldsymbol{0} & \boldsymbol{R}_{\text{mru}_2} \end{bmatrix}$
  $\boldsymbol{y}_k \leftarrow \begin{bmatrix} \boldsymbol{z}_{\text{mru}_1} - \boldsymbol{h}_{\text{mru}_1}(\hat{\boldsymbol{x}}_{k|k-1}) \\ \boldsymbol{z}_{\text{mru}_2} - \boldsymbol{h}_{\text{mru}_2}(\hat{\boldsymbol{x}}_{k|k-1}) \end{bmatrix}$
  if Visual sight is possible **then**
    $\boldsymbol{H}_k \leftarrow \begin{bmatrix} \boldsymbol{H}_k \\ \boldsymbol{H}_{\text{visual},k} \end{bmatrix} \quad \boldsymbol{R}_k \leftarrow \begin{bmatrix} \boldsymbol{R}_k & \boldsymbol{0} \\ \boldsymbol{0} & \boldsymbol{R}_{\text{visual}} \end{bmatrix}$
    $\boldsymbol{y}_k \leftarrow \begin{bmatrix} \boldsymbol{y}_k \\ \boldsymbol{z}_{\text{visual}} - \boldsymbol{h}_{\text{visual}}(\hat{\boldsymbol{x}}_{k|k-1}) \end{bmatrix}$
  end if
  if GNNS available **then**
    $\boldsymbol{H}_k \leftarrow \begin{bmatrix} \boldsymbol{H}_k \\ \boldsymbol{H}_{\text{gnns},k} \end{bmatrix} \quad \boldsymbol{R}_k \leftarrow \begin{bmatrix} \boldsymbol{R}_k & \boldsymbol{0} \\ \boldsymbol{0} & \boldsymbol{R}_{\text{gnns}} \end{bmatrix}$
    $\boldsymbol{y}_k \leftarrow \begin{bmatrix} \boldsymbol{y}_k \\ \boldsymbol{z}_{\text{gnss}} - \boldsymbol{h}_{\text{gnns}}(\hat{\boldsymbol{x}}_{k|k-1}) \end{bmatrix}$
  end if
  // Innovation covariance and near optimal Kalman gain
  $\boldsymbol{S}_k \leftarrow \boldsymbol{H}_k \boldsymbol{P}_{k|k-1} \boldsymbol{H}_k^T + \boldsymbol{R_k}$
  $\boldsymbol{K}_k \leftarrow \boldsymbol{P}_{k|k-1} \boldsymbol{H}_k^T \boldsymbol{S}_k^{-1}$

  // Update state estimate and state covariance
  $\hat{\boldsymbol{x}}_{k|k} \leftarrow \hat{\boldsymbol{x}}_{k|k-1} + \boldsymbol{K}_k \boldsymbol{y}_k$
  $\boldsymbol{P}_{k|k} \leftarrow (\boldsymbol{I} - \boldsymbol{K}_k \boldsymbol{H}_k) \boldsymbol{P}_{k|k-1}$
  $k \leftarrow k + 1$
end loop

The presented algorithm assumes that both MRUs are available for each EKF iteration k, and appends the other sensor measurements represented by the GNSS system or the visual sensor if these measurements are available. This implementation adds a certain degree of redundancy since the process is modeled in such a manner that the heading offset is more or less constant. As a result, the estimation can rely only on the inertial MRU measurements for small time periods, and hence also allow for asynchronous correction data acquired from both the visual sensor and the GNSS system.

The tuning of the process and measurement covariance matrices $\boldsymbol{Q}$ and $\boldsymbol{R}_s$ will not

be discussed in details here, partly because they are discussed throughout the appended papers, and because this chapter aims at presenting the theory and not account for sensor-specific parameters which will vary from sensor to sensor. Anyway, as basic tuning principle the following two statements can be used to tune the covariance matrices:

- $\boldsymbol{Q} < \boldsymbol{R} \rightarrow$ The EKF output tends to follow the process/model more than the measured signals i.e. the measurements are trusted less than the process.
- $\boldsymbol{Q} > \boldsymbol{R} \rightarrow$ The EKF output tends to follow the measurements more than the process i.e. the measurements are assumed to be more accurate.

2.6 Crane Operator Assistant

This section will finally propose a kinematic controller for the offshore crane in a ship-to-ship load transfer situation. It is worth mentioning that the content of this section is currently not published in any of the previous appended papers, and hence will also be elaborated in more detail in comparison to the previous sections of this chapter. Reusing the knowledge discussed earlier related to kinematics, dynamics, and state estimation, a crane operator assistant is developed to reduce the suspended load swing angles and automatically adjust the wire length so that the hook/load is kept in a fixed distance above the second ship deck. Still, the crane operator is required to operate the crane, but the assisting system will continuously assist the operator by slightly manipulating the operator input in real-time. The expected outcome of such assisting system is reduced risk, higher repeatability and increased operational efficiency in ship-to-ship operations.

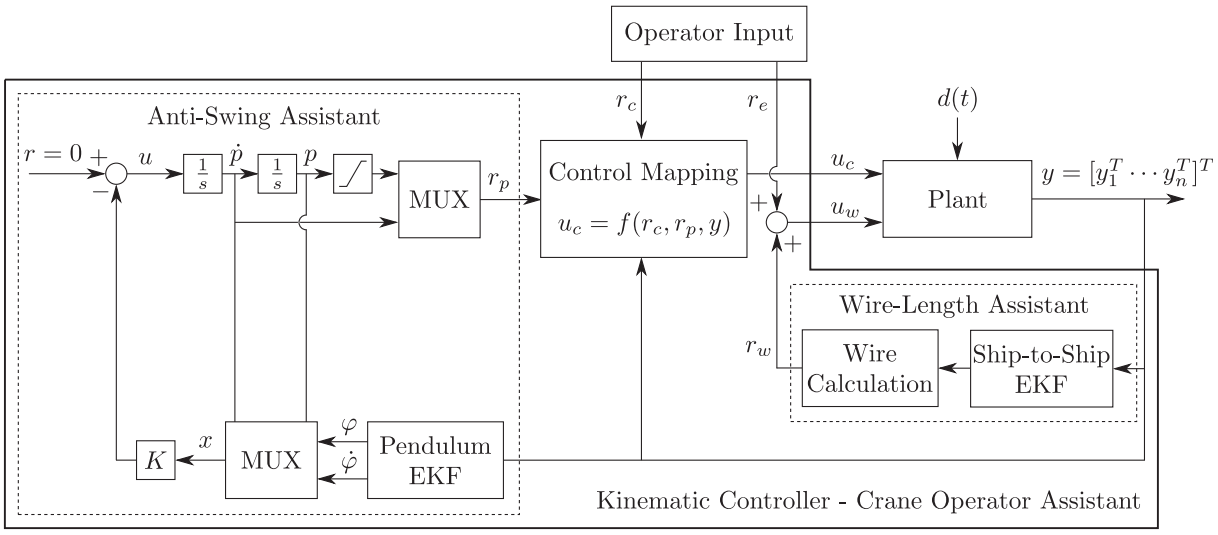

Figure 2.9: Schematic of the two assistant systems which aim at reducing the load swinging (Anti-Swing Assistant) and keeping the load/hook in a fixed distance above the secondary ship deck (Wire-Length Assistant).

Figure 2.9 illustrates the implementation of the two crane operator assistants where the plant represents the ships, the crane, the winch system, and the transferred load. The

plant has two main inputs; one for the crane $\boldsymbol{u}_c$ and one for the winch $\boldsymbol{u}_w$ which are:

$$\boldsymbol{u}_c = \begin{bmatrix} \boldsymbol{q}_r \\ \dot{\boldsymbol{q}}_r \end{bmatrix}, \quad \text{and} \quad \boldsymbol{u}_w = \begin{bmatrix} L_r \\ \dot{L}_r \end{bmatrix} \tag{2.49}$$

where the subscript r indicates that the two plant inputs are the control reference input to the already existing closed-loop controllers operating the crane and the winch. This means that there is no possibility to control the forces of the respective machines, which only allows for manipulation of the two input trajectories consisting of position and velocity inputs. The control task of the of the two crane operator assistants are the following:

Wire-Length Assistant: The winch length should automatically be adjusted to keep the load in a fixed distance above the secondary ship deck, even though both the ships move independently due to external environmental disturbances such as wind, and waves. The operator can at any time adjust the extra winch reference $\boldsymbol{r}_e$ to increase or decrease the distance between the ship deck and the transferred load.

Anti-Swing Assistant: The swing angles of the suspended load shall be reduced by continuously generating an additional reference $\boldsymbol{r}_p$ which is added on top of the desired crane reference $\boldsymbol{r}_c$ defined by the operator. This system shall; correct the path when the operator tries to move the crane from A to B so that the movement does not generate swing in the load, reject or minimize the swing motions caused by the ship movement, and reduce the swing-motion caused by direct disturbances to the suspended load, such as wind forces or physical collisions etc.

The two operator inputs $\boldsymbol{r}_c$ and $\boldsymbol{r}_e$ contain the following signals:

$$\boldsymbol{r}_c = \begin{bmatrix} \boldsymbol{q}_d \\ \dot{\boldsymbol{q}}_d \end{bmatrix}, \quad \text{and} \quad \boldsymbol{r}_e = \begin{bmatrix} L_e \\ \dot{L}_e \end{bmatrix} \tag{2.50}$$

where $\boldsymbol{q}_d$ and $\dot{\boldsymbol{q}}_d$ are the desired crane position and velocity of the controllable degrees-of-freedom, and L_e and $\dot{L}_e$ are the extra wire length and velocity used to adjust the distance between the secondary ship deck and the suspended load. This additional input is also supposed to account for the physical size of the load e.g. the crane operator will adjust the $\boldsymbol{r}_e$ input manually to account for the physical size of the load.

The plant is heavily non-linear caused by means of non-linear kinematics in the crane structure, and hence also the hydraulic actuation system itself. Reusing the knowledge about the non-linear kinematics described in Section 2.4 and the ship body kinematics defined in Section 2.3, a control mapping is used to implement the anti-swing system which aims at slightly correcting the desired trajectory described by continuously calculating an additional correction trajectory described as:

$$\boldsymbol{r}_p = \begin{bmatrix} \boldsymbol{p} \\ \dot{\boldsymbol{p}} \end{bmatrix} = \begin{bmatrix} p_x \\ p_y \\ \dot{p}_x \\ \dot{p}_y \end{bmatrix} \tag{2.51}$$

where the additional position $\boldsymbol{p}$ and velocity $\dot{\boldsymbol{p}}$ are used to adjust the desired crane trajectory slightly in order to reduce the suspended load swing angles in real-time. The anti-swing correction term $\boldsymbol{r}_p$ is supposed to move the crane in the x- and y-direction in the heading coordinate system $\{n_1\}$ depending of the current situation of the load which has to be measured using an observer. Both the calculation of the correction term $\boldsymbol{r}_p$ and the modeling of the observer will be discussed in the next subsections.

All the feedback signals of the whole plant are augmented in the generalized feedback vector $\boldsymbol{y}$ where it assumed that the available sensors are capable of measuring the following states:

$$\boldsymbol{y} = \begin{bmatrix} \boldsymbol{\eta}_1^T & \boldsymbol{v}_1^T & \boldsymbol{\eta}_2^T & \boldsymbol{v}_2^T & \boldsymbol{q}^T & \dot{\boldsymbol{q}}^T & L_w & \dot{L}_w & \boldsymbol{p}_h^T \end{bmatrix}^T \tag{2.52}$$

where $\boldsymbol{\eta}$ and $\boldsymbol{v}$ are the position and velocity of both the ships, $\boldsymbol{q}$ and $\dot{\boldsymbol{q}}$ represent the crane feedback position and velocity, L_w and $\dot{L}_w$ are the wire length and velocity, and finally $\boldsymbol{p}_h$ is the measured hook position. The next subsections of this section will elaborate on the implementation of the crane operator assistant, and in the end, a final experimental validation of the proposed method will be presented using results acquired from the motion laboratory.

2.6.1 Kinematic Control Mapping

The control mapping function aims at calculating a crane control input $\boldsymbol{u}_c$ based on the generalized feedback signal $\boldsymbol{y}$, the anti-swing correction term $\boldsymbol{r}_p$ and the crane operator input $\boldsymbol{r}_c$. The calculated crane input $\boldsymbol{u}_c$ aims at both stabilizing the suspended load dynamics while simultaneously trying to meet the desired crane motion prescribed by the operator as illustrated by Figure 2.9. The resulting non-linear control mapping is implemented using:

$$\boldsymbol{u}_c = \begin{bmatrix} \boldsymbol{q}_r \\ \dot{\boldsymbol{q}}_r \end{bmatrix} = \underbrace{\begin{bmatrix} \boldsymbol{f}_{IK}(\boldsymbol{r}_{AC}^c + \boldsymbol{r}_{AS}^c) \\ \boldsymbol{J}_{\boldsymbol{q}}^{-1}(\boldsymbol{q}_r)(\dot{\boldsymbol{r}}_{AC}^c + \dot{\boldsymbol{r}}_{AS}^c) \end{bmatrix}}_{\boldsymbol{f}(\boldsymbol{r}_c, \boldsymbol{r}_p, \boldsymbol{y})} \tag{2.53}$$

where:

$$\boldsymbol{r}_{AC} = \begin{bmatrix} \boldsymbol{r}_{AC}^c \\ \dot{\boldsymbol{r}}_{AC}^c \end{bmatrix}, \quad \text{and} \quad \boldsymbol{r}_{AS} = \begin{bmatrix} \boldsymbol{r}_{AS}^c \\ \dot{\boldsymbol{r}}_{AS}^c \end{bmatrix} \tag{2.54}$$

are the attitude corrected crane reference $\boldsymbol{r}_{AC}$, and $\boldsymbol{r}_{AS}$ is the additional anti-swing correction reference used to stabilize the load motion. The attitude correction reference aims at modifying the input crane reference $\boldsymbol{r}_c$ such that the roll, pitch and yaw motions of the ship will not influence the horizontal crane tip motion, hence only the surge and sway will disturb the suspended load. The attitude corrected crane reference $\boldsymbol{r}_{AC}$ is derived by:

$$\underbrace{\begin{bmatrix} \boldsymbol{r}_{AC}^c \\ \dot{\boldsymbol{r}}_{AC}^c \end{bmatrix}}_{\boldsymbol{r}_{AC}} = \begin{bmatrix} \boldsymbol{R}_{n_1}^c \boldsymbol{R}_c^{b_1} \boldsymbol{f}_{FK}(\boldsymbol{q}_d) \\ \dot{\boldsymbol{R}}_{n_1}^c \boldsymbol{R}_c^{b_1} \boldsymbol{f}_{FK}(\boldsymbol{q}_d) + \boldsymbol{R}_{n_1}^c \boldsymbol{R}_c^{b_1} \boldsymbol{J}_{\boldsymbol{q}}(\boldsymbol{q}_d)\dot{\boldsymbol{q}}_d \end{bmatrix} = \underbrace{\begin{bmatrix} \boldsymbol{R}_{n_1}^c & \boldsymbol{0} \\ \dot{\boldsymbol{R}}_{n_1}^c & \boldsymbol{R}_{n_1}^c \end{bmatrix}}_{\boldsymbol{T}_{n_1}^c(\boldsymbol{y})} \underbrace{\begin{bmatrix} \boldsymbol{R}_c^{b_1} \boldsymbol{f}_{FK}(\boldsymbol{q}_d) \\ \boldsymbol{R}_c^{b_1} \boldsymbol{J}_{\boldsymbol{q}}(\boldsymbol{q}_d)\dot{\boldsymbol{q}}_d \end{bmatrix}}_{\boldsymbol{f}(\boldsymbol{r}_c)} \tag{2.55}$$

where $\boldsymbol{T}_{n_1}^{c}(\boldsymbol{y})$ is the matrix used to transform $\boldsymbol{f}(\boldsymbol{r}_c)$ represented in $\{n_1\}$ back to $\{c\}$. The two matrices $\boldsymbol{R}_{n_1}^{c}$ and $\dot{\boldsymbol{R}}_{n_1}^{c}$ are calculated using the MRU feedback, and $\boldsymbol{R}_{c}^{b_1}$ is the already known crane orientation onto the main ship. The additional anti-swing reference $\boldsymbol{r}_{AS}$ is derived as:

$$\underbrace{\begin{bmatrix}\boldsymbol{r}_{AS}^{c}\\ \dot{\boldsymbol{r}}_{AS}^{c}\end{bmatrix}}_{\boldsymbol{r}_{AS}} = \boldsymbol{T}_{n_1}^{c}(\boldsymbol{y}) \begin{bmatrix}\boldsymbol{p}\\ 0\\ \dot{\boldsymbol{p}}\\ 0\end{bmatrix} \tag{2.56}$$

which allows for the anti-swing input $\boldsymbol{r}_p$ to be included and hence also finally manipulate the controllable joints so that the crane tip will try to dampen out the swinging load motion.

2.6.2 Wire-Length Assistant

In this section, the required length of the wire between the wire exit point and the hook is to be calculated as a result of being capable of observing the ship-to-ship motions as described in section 2.5.

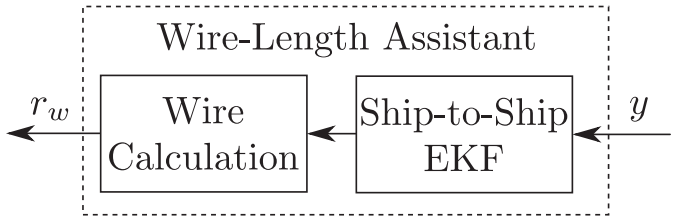

Figure 2.10: Snapshot from Figure 2.9 illustrating the wire length assistant used to calculate the correct length of the wire to keep the hook in a fixed position above the secondary ship deck during ship-to-ship load transfer.

The goal is to derive the analytical functions which can be used to calculate the required wire length and velocity as a function of the estimated ship-to-ship state vector $\hat{\boldsymbol{x}}$. The wire length and velocity are calculated for the situation when the load is hanging straight downwards, meaning in the z-direction of the coordinate system $\{n_1\}$.

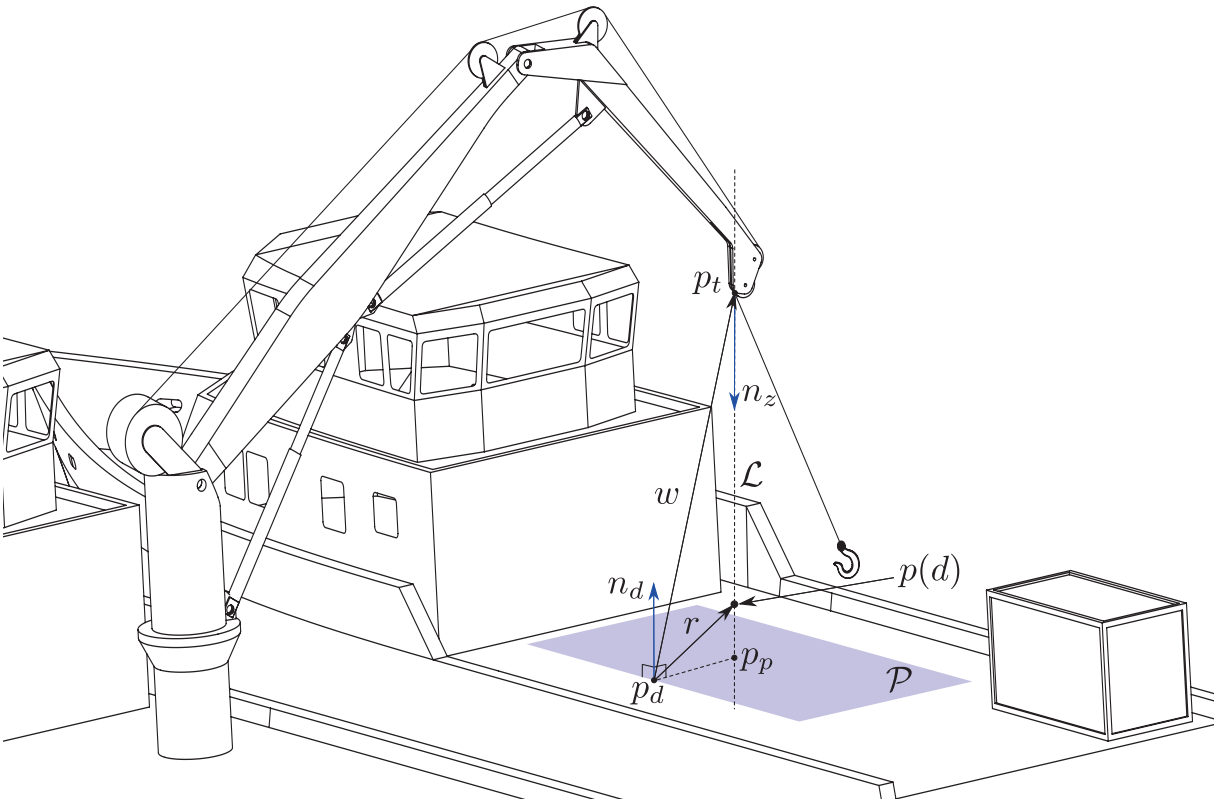

Figure 2.11: Illustration of the wire length calculation between the tool point $\boldsymbol{p}_t$ and projected point $\boldsymbol{p}_p$ located on secondary ship deck plane.

To calculate the wire length, the line-plane intersection is used as a fundamental understanding to form the required equations, and the geometric problem is illustrated by Figure 2.11. In a line-plane intersection, the line $\mathcal{L}$ is either parallel to the plane $\mathcal{P}$, or it intersects the plane in one single unique point $\boldsymbol{p_p}$ as shown in the figure. The plane $\mathcal{P}$ representing the ship deck is defined by the point $\boldsymbol{p_d}$ and the normal vector $\boldsymbol{n}_d$. A parametrization of the point laying on the line segment $\mathcal{L}$ is given by:

$$\boldsymbol{p}(d) = \boldsymbol{w} + d\boldsymbol{n}_z \tag{2.57}$$

where d is the distance between the crane tip and the point $\boldsymbol{p}(d)$. At the point of line-plane intersection, the vector $\boldsymbol{r} = \boldsymbol{p}(d) - \boldsymbol{p}_d$ is perpendicular to the plane normal vector $\boldsymbol{n}_d$ i.e.

$$\boldsymbol{r} \cdot \boldsymbol{n}_d = \boldsymbol{w} \cdot \boldsymbol{n}_d + d\boldsymbol{n}_z \cdot \boldsymbol{n}_d = 0 \tag{2.58}$$

where $\cdot$ indicates the vector dot product. Solving this equation for the distance d:

$$d = \frac{-\boldsymbol{w} \cdot \boldsymbol{n}_d}{\boldsymbol{n}_z \cdot \boldsymbol{n}_d} \tag{2.59}$$

will describe the length between the crane tip $\boldsymbol{p}_t$ and the projected point $\boldsymbol{p_p}$ in the direction of $\boldsymbol{n}_z$. Defining $a = \boldsymbol{w} \cdot \boldsymbol{n}_d$ and $b = \boldsymbol{n}_z \cdot \boldsymbol{n}_d$, the wire length L and velocity $\dot{L}$ are calculated

using:

$$L = -\frac{a}{b} \tag{2.60}$$

$$\dot{L} = \frac{a\dot{b}}{b^2} - \frac{\dot{a}}{b} \tag{2.61}$$

where the time derivatives of a and b are:

$$\dot{a} = \dot{\boldsymbol{w}} \cdot \boldsymbol{n}_d + \boldsymbol{w} \cdot \dot{\boldsymbol{n}}_d \tag{2.62}$$

$$\dot{b} = \boldsymbol{n}_z \cdot \dot{\boldsymbol{n}}_d \tag{2.63}$$

since $\dot{\boldsymbol{n}}_z = \boldsymbol{0}$. The next step is to define the vectors $\boldsymbol{w}$, $\boldsymbol{n}_d$, and $\boldsymbol{n}_z$ as a function of the estimated ship-to-ship states $\boldsymbol{x}$ defined in Eq. 2.35 and the crane feedback. The vectors are calculated using:

$$\boldsymbol{w} = \boldsymbol{r}_{t/d}^{n_1} = \underbrace{\boldsymbol{r}_{b_1/n_1}^{n_1} + \boldsymbol{R}_{b_1}^{n_1}\left(\boldsymbol{r}_{c/b_1}^{b_1} + \boldsymbol{R}_{c}^{b_1}\boldsymbol{r}_{t/c}^{c}\right)}_{\boldsymbol{r}_{t/n_1}^{n_1}} - \underbrace{\left(\boldsymbol{r}_{n_2/n_1}^{n_1} + \boldsymbol{R}_{n_2}^{n_1}\left(\boldsymbol{r}_{b_2/n_2}^{n_2} + \boldsymbol{R}_{b_2}^{n_2}\boldsymbol{r}_{d/b_2}^{b_2}\right)\right)}_{\boldsymbol{r}_{d/n_1}^{n_1}} \tag{2.64}$$

$$\boldsymbol{n}_d = -\boldsymbol{z}_{b_2}^{n_1} = -\left(\begin{bmatrix}0 & 0 & 1\end{bmatrix}\left(\boldsymbol{R}_{n_2}^{n_1}\boldsymbol{R}_{b_2}^{n_2}\right)^T\right)^T \tag{2.65}$$

$$\tag{2.66}$$

$$\boldsymbol{n}_z = \boldsymbol{z}_{n_1}^{n_1} = \begin{bmatrix}0 & 0 & 1\end{bmatrix}^T \tag{2.67}$$

where $\boldsymbol{z}_{b_2}^{n_1}$ is the z-axis of ship body 2 $\{b_2\}$, and $\boldsymbol{z}_{n_1}^{n_1}$ is the z-axis of heading coordinate $\{n_1\}$. The time derivatives of $\boldsymbol{w}$, $\boldsymbol{n}_d$ and $\boldsymbol{n}_z$ are found from direct time differentiation of the equations and will not be elaborated in details.

2.6.3 Anti-Swing Assistant

This section will present a method to dampen out the swing angles of the suspended load by creating a correction trajectory $\boldsymbol{r}_p$ which will try to move the crane in such manner that the suspended load is stabilized. To carry out this task, the pendulum angles have to be known, which leads to the use of an observer to estimate the angles based on measurements of the hook motion. Using the estimated swing-angles, an additional reference input will be calculated using a state feedback approach where the observed angles and angular velocities are used to generate the correction trajectory.

2.6.3.1 Load Kinematics

The position of the crane hook $\boldsymbol{p}_h$ relative to the crane tip $\boldsymbol{p}_t$ is modeled on the basis of the two swing angles φ_1 and φ_2 as shown in Figure 2.12.

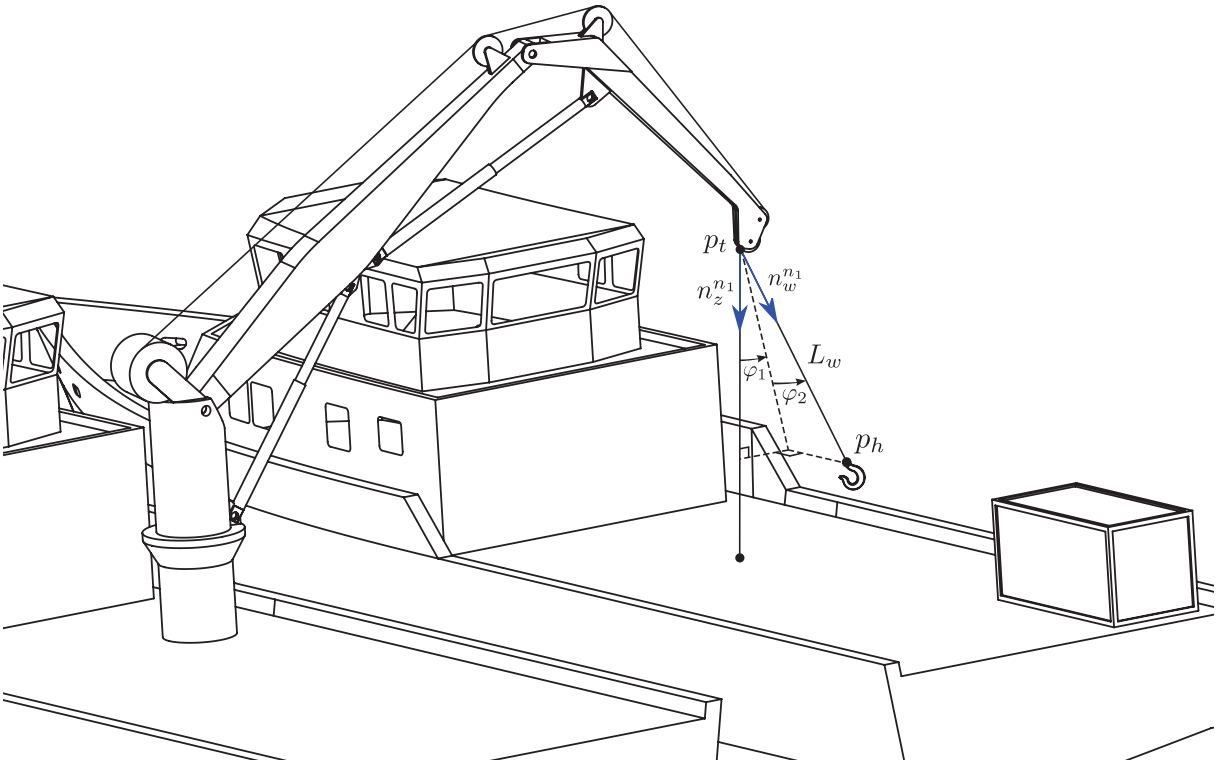

Figure 2.12: Illustration of the suspended load swing angles φ_1 and φ_2 during ship-to-ship operation.

The suspended load is modeled as spherical pendulum, and $\{n_1\}$ is chosen to be the reference coordinate system since both the movement of the crane and the ship are affecting the acceleration of the crane tool tip, and hence have to be included in the description of the crane tip acceleration term. The crane tip acceleration is derived from taking the time derivative of the crane tip position given by:

$$\boldsymbol{r}_{t/n_1}^{n_1} = \boldsymbol{r}_{b_1/n_1}^{n_1} + \boldsymbol{R}_{b_1}^{n_1}\left(\boldsymbol{r}_{c/b_1}^{b_1} + \boldsymbol{R}_{c}^{b_1}\boldsymbol{r}_{t/c}^{c}\right) \tag{2.68}$$

where $\boldsymbol{r}_{t/n_1}^{n_1}$ is the crane tip position given in $\{n_1\}$, $\boldsymbol{r}_{c/b_1}^{b_1}$ and $\boldsymbol{R}_{c}^{b_1}$ are the crane position and orientation onto the main ship, and $\boldsymbol{r}_{t/c}^{c}$ is the crane tip position given in $\{c\}$. The resulting crane tip velocity is:

$$\dot{\boldsymbol{r}}_{t/n_1}^{n_1} = \dot{\boldsymbol{r}}_{b_1/n_1}^{n_1} + \dot{\boldsymbol{R}}_{b_1}^{n_1}\left(\boldsymbol{r}_{c/b_1}^{b_1} + \boldsymbol{R}_{c}^{b_1}\boldsymbol{r}_{t/c}^{c}\right) + \boldsymbol{R}_{b_1}^{n_1}\boldsymbol{R}_{c}^{b_1}\dot{\boldsymbol{r}}_{t/c}^{c}, \tag{2.69}$$

where:

$$\dot{\boldsymbol{R}}_{b_1}^{n_1} = \boldsymbol{R}_{b_1}^{n_1}\boldsymbol{S}(\boldsymbol{\omega}_{b_1/n_1}^{b_1}). \tag{2.70}$$

It is assumed that the ship is completely rigid, which leads to the time derivatives of the crane position $\dot{\boldsymbol{r}}_{c/b_1}^{b_1}$ and the orientation $\dot{\boldsymbol{R}}_{c}^{b_1}$ are both equal to zero. The crane tip acceleration $\ddot{\boldsymbol{r}}_{t/n_1}^{n_1}$ is finally derived by:

$$\ddot{\boldsymbol{r}}_{t/n_1}^{n_1} = \ddot{\boldsymbol{r}}_{b_1/n_1}^{n_1} + \ddot{\boldsymbol{R}}_{b_1}^{n_1}\left(\boldsymbol{r}_{c/b_1}^{b_1} + \boldsymbol{R}_{c}^{b_1}\boldsymbol{r}_{t/c}^{c}\right) + 2\dot{\boldsymbol{R}}_{b_1}^{n_1}\boldsymbol{R}_{c}^{b_1}\dot{\boldsymbol{r}}_{t/c}^{c} + \boldsymbol{R}_{b_1}^{n_1}\boldsymbol{R}_{c}^{b_1}\ddot{\boldsymbol{r}}_{t/c}^{c}, \tag{2.71}$$

where:

$$\ddot{\boldsymbol{R}}_{b_1}^{n_1} = \boldsymbol{R}_{b_1}^{n_1}\boldsymbol{S}(\boldsymbol{\omega}_{b_1/n_1}^{b_1})\boldsymbol{S}(\boldsymbol{\omega}_{b_1/n_1}^{b_1}) + \boldsymbol{R}_{b_1}^{n_1}\boldsymbol{S}(\dot{\boldsymbol{\omega}}_{b_1/n_1}^{b_1}). \tag{2.72}$$

The suspended hook position $\boldsymbol{r}_{h/n_1}^{n_1}$ is also required to model the pendulum dynamics later on. It is desirable to parametrize the hook movement as a function of the crane tip movement and the two swing angles φ_1 and φ_2. This is motivated from the fact that a control system could be used to manipulate the crane movement in such a manner that the swing angles are reduced to zero i.e. the suspended load is hanging straight downward with zero influence of the gravity causing the load to swing. The hook position is parametrized as:

$$\boldsymbol{r}_{h/n_1}^{n_1} = \boldsymbol{r}_{t/n_1}^{n_1} + L_w \underbrace{\begin{bmatrix} -\sin(\varphi_1) \\ \cos(\varphi_1)\sin(\varphi_2) \\ \cos(\varphi_1)\cos(\varphi_2) \end{bmatrix}}_{\boldsymbol{n}_w^{n_1}} = \boldsymbol{f}(\boldsymbol{r}_{t/n_1}^{n_1}, \boldsymbol{\varphi}, L_w), \quad \boldsymbol{\varphi} = [\varphi_1, \varphi_2]^T \tag{2.73}$$

where L_w is the wire length, $\boldsymbol{n}_w^{n_1}$ is the unitary directional vector pointing along the wire, and $\boldsymbol{\varphi}$ is the vector describing the two possible swing angles of the suspended load. The hook velocity $\dot{\boldsymbol{r}}_{h/n_1}^{n_1}$ is found from directly taking the time derivative of the hook position:

$$\dot{\boldsymbol{r}}_{h/n_1}^{n_1} = \dot{\boldsymbol{r}}_{t/n_1}^{n_1} + \dot{L}_w \begin{bmatrix} -\sin(\varphi_1) \\ \cos(\varphi_1)\sin(\varphi_2) \\ \cos(\varphi_1)\cos(\varphi_2) \end{bmatrix} + L_w \begin{bmatrix} -\dot{\varphi}_1\cos(\varphi_1) \\ -\dot{\varphi}_1\sin(\varphi_1)\sin(\varphi_2) + \dot{\varphi}_2\cos(\varphi_1)\cos(\varphi_2) \\ -\dot{\varphi}_1\sin(\varphi_1)\cos(\varphi_2) - \dot{\varphi}_2\cos(\varphi_1)\sin(\varphi_2) \end{bmatrix}. \tag{2.74}$$

2.6.3.2 Load Dynamics

The dynamics of the suspended pendulum will be derived using the Euler-Lagrange formulation, and the following assumptions are made to simplify the modeling of the dynamics. It is assumed that the masses of the ship m_s, crane m_c, the transported load m_L, and the wire m_w are related to each other according to:

$$m_s >> m_c >> m_L >> m_w \tag{2.75}$$

which will imply that the more heavy component dominates the motion of the less heavy component, and that the suspended load can be simply modeled as a spherical pendulum with massless wire and a point mass connected to the hook. The potential energy $\mathcal{P}$ and the kinetic energy $\mathcal{K}$ of the suspended load are:

$$\mathcal{P} = m_L g(L_w - L_w\cos(\varphi_1)\cos(\varphi_2)) \tag{2.76}$$

$$\mathcal{K} = \frac{1}{2}m_L\left(\dot{\boldsymbol{r}}_{h/n_1}^{n_1}\right)^T\dot{\boldsymbol{r}}_{h/n_1}^{n_1} \tag{2.77}$$

where the method used to describe energy terms are inherited from [49]. By using the two energy terms given above, the suspended load dynamics is derived from applying the Euler-Lagrange formulation to the Lagrangian which is defined:

$$\mathcal{L} = \mathcal{K} - \mathcal{P}. \tag{2.78}$$

The differential equation is then found as:

$$\frac{d}{dt}\frac{\partial \mathcal{L}}{\partial \dot{\boldsymbol{\varphi}}} - \frac{\partial \mathcal{L}}{\partial \boldsymbol{\varphi}} = -c\boldsymbol{\varphi}, \qquad \boldsymbol{\varphi} = \begin{bmatrix}\varphi_1 & \varphi_2\end{bmatrix}^T \tag{2.79}$$

where $c\boldsymbol{\varphi}$ is the damping in the wire exit point. To generate the differential equations, the Symbolic Toolbox of MATLAB has been used to derive the resulting differential equations:

$$\begin{aligned}
\ddot{\varphi}_1 &= -c\dot{\varphi}_1 - (L_w \cos(\varphi_1)\sin(\varphi_1)\dot{\varphi}_2^2 + 2\dot{L}_w\dot{\varphi}_1 - \ddot{x}^{n_1}_{t/n_1}\cos(\varphi_1) \\
&\quad + g\cos(\varphi_2)\sin(\varphi_1) - \ddot{z}^{n_1}_{t/n_1}\cos(\varphi_2)\sin(\varphi_1) - \ddot{y}^{n_1}_{t/n_1}\sin(\varphi_1)\sin(\varphi_2))/L_w \\
\ddot{\varphi}_2 &= -c\dot{\varphi}_2 - (\ddot{y}^{n_1}_{t/n_1}\cos(\varphi_2) + g\sin(\varphi_2) - \ddot{z}^{n_1}_{t/n_1}\sin(\varphi_2) \\
&\quad + 2\dot{L}_w\dot{\varphi}_2\cos(\varphi_1) - 2L_w\dot{\varphi}_1\dot{\varphi}_2\sin(\varphi_1))/(L_w\cos(\varphi_1)) \\
\ddot{\boldsymbol{\varphi}} &= \begin{bmatrix}\ddot{\varphi}_1 \\ \ddot{\varphi}_2\end{bmatrix} = \boldsymbol{f}_{\text{load}}(\boldsymbol{\varphi}, \dot{\boldsymbol{\varphi}}, L_w, \dot{L}_w, c, g, \ddot{\boldsymbol{r}}^{n_1}_{t/n_1}), \quad \ddot{\boldsymbol{r}}^{n_1}_{t/n_1} = \begin{bmatrix}\ddot{x}^{n_1}_{t/n_1} & \ddot{y}^{n_1}_{t/n_1} & \ddot{z}^{n_1}_{t/n_1}\end{bmatrix}^T
\end{aligned} \tag{2.80}$$

where $\boldsymbol{\varphi}$ is the pendulum angles, $\dot{\boldsymbol{\varphi}}$ is the angular velocity, $\ddot{\boldsymbol{\varphi}}$ is the angular acceleration, L_w is the wire length between the crane tip and the load, $\dot{L}_w$ is the velocity of the wire, c is the damping in the wire exit point of the crane tip, g is the gravity constant, and finally $\ddot{\boldsymbol{r}}^{n_1}_{t/n_1}$ is the acceleration of the crane tip given in $\{n_1\}$.

2.6.3.3 Load Observer

In the previous two sections, both the kinematics and the dynamics of the pendulum were presented. In this section, these equations will be reused to form the process and measurement model which will be used to observe suspended load motion in real-time. The corresponding state vector of the suspended load dynamics to be observed is:

$$\boldsymbol{x}_p = \begin{bmatrix} \boldsymbol{r}^{n_1}_{t/n_1} \\ \dot{\boldsymbol{r}}^{n_1}_{t/n_1} \\ \ddot{\boldsymbol{r}}^{n_1}_{t/n_1} \\ \boldsymbol{\varphi} \\ \dot{\boldsymbol{\varphi}} \\ L_w \\ \dot{L}_w \\ c \end{bmatrix} \tag{2.81}$$

where the different components of the state vector are discussed previously. The accompanying process model is modeled as:

$$\dot{\boldsymbol{x}}_p = \underbrace{\begin{bmatrix} \dot{\boldsymbol{r}}^{n_1}_{t/n_1} \\ \ddot{\boldsymbol{r}}^{n_1}_{t/n_1} \\ \boldsymbol{0} \\ \dot{\boldsymbol{\varphi}} \\ \boldsymbol{f}_{\text{load}}(\boldsymbol{\varphi}, \dot{\boldsymbol{\varphi}}, L_w, \dot{L}_w, c, g, \ddot{\boldsymbol{r}}^{n_1}_{t/n_1}) \\ \dot{L}_w \\ 0 \\ 0 \end{bmatrix}}_{\boldsymbol{f}_L(\boldsymbol{x_L})} + \boldsymbol{w}_p \tag{2.82}$$

where the pendulum differential equation $\boldsymbol{f}_{\text{load}}(\boldsymbol{\varphi}, \dot{\boldsymbol{\varphi}}, L_w, \dot{L}_w, c, g, \ddot{\boldsymbol{r}}^{n_1}_{t/n_1})$ is defined by Eq. (2.80). Furthermore, the corresponding measurement model is given as:

$$\boldsymbol{z}_p = \boldsymbol{h}_p(\boldsymbol{x}_p) = \begin{bmatrix} \boldsymbol{r}^{n_1}_{t/n_1} \\ \dot{\boldsymbol{r}}^{n_1}_{t/n_1} \\ L_w \\ \dot{L}_w \\ \boldsymbol{f}(\boldsymbol{r}^{n_1}_{t/n_1}, \boldsymbol{\varphi}, L_w) \end{bmatrix} + \boldsymbol{v}_p \tag{2.83}$$

where $\boldsymbol{z}_p$ is the measurement vector which augments the crane tip position $\boldsymbol{r}^{n_1}_{t/n_1}$, crane tip velocity $\dot{\boldsymbol{r}}^{n_1}_{t/n_1}$, the wire length L_w, wire velocity $\dot{L}_w$, and finally the hook position $\boldsymbol{r}^{n_1}_{h/n_1} = \boldsymbol{f}(\boldsymbol{r}^{n_1}_{t/n_1}, \boldsymbol{\varphi}, L_w)$ which is derived in Eq. (2.73). It is hereby assumed that the measurements are carried out in the heading coordinate $\{n_1\}$, which may not be realistic since no sensor can be attached to this coordinate system since it does not represent a physical body. Anyway, it can be useful to form the measurement function to be a general function like the one presented here and instead transform the measurement carried out in another coordinate to yield in the heading coordinate instead. E.g. if the hook were measured by sensor placed on $\{b_1\}$, the measurements could be transformed to $\{n_1\}$ using:

$$\boldsymbol{r}^{n_1}_{h/n_1} = \boldsymbol{r}^{n_1}_{b_1} + \boldsymbol{R}^{n_1}_{b_1} \boldsymbol{p}^{b_1}_h \tag{2.84}$$

where $\boldsymbol{p}^{b_1}_h$ is the measured hook position in $\{b_1\}$. By reusing the kinematic equations discussed throughout this chapter, the sensor used to measure the crane hook could now be placed on any physical body. This body could be the crane tower, main boom or the jib for instance, and hence the same observer implementation would be valid as long as the sensor measurement is transformed correctly to yield in the heading coordinate $\{n_1\}$. The presented process and measurement model can now be used to observe the pendulum dynamics and hence realized using different state estimation techniques, but the standard EKF will most likely be the most computational efficient for real-time implementation on an industrial control unit like a PLC. Alternatively, other methods to measure the pendulum angles could be based on vision [50, 51] or a potentiometer instrument [52] attached directly to the crane tip could be considered instead.

2.6.3.4 Anti-Swing using LQR State Feedback

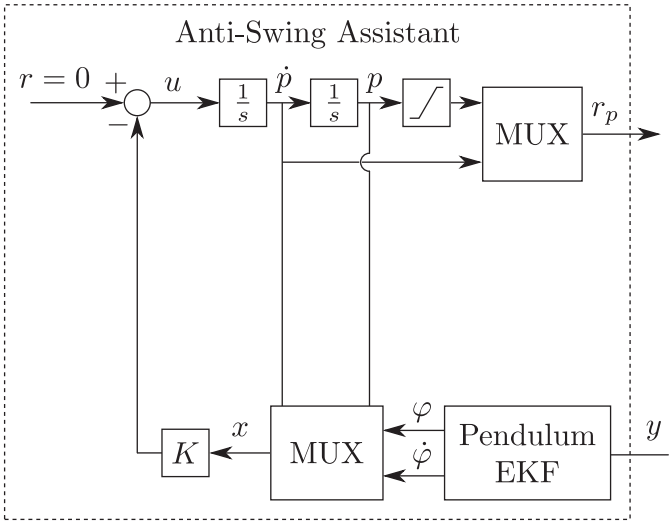

Figure 2.13: Snapshot from Figure 2.9 illustrating the anti-swing assistant used to correct the crane trajectory input reference in case of non-zero swing angles.

The anti-swing assistant which is illustrated in Figure 2.13 is supposed to generate an additional input trajectory $\boldsymbol{r}_p$, which aims at continuously reducing the swing angles $\boldsymbol{\varphi}$ as much as possible without the need to model the whole process including the complex crane dynamics, and hence making the anti-swing system more modular compared to using traditional control strategies which is heavily dependent to the crane dynamics.

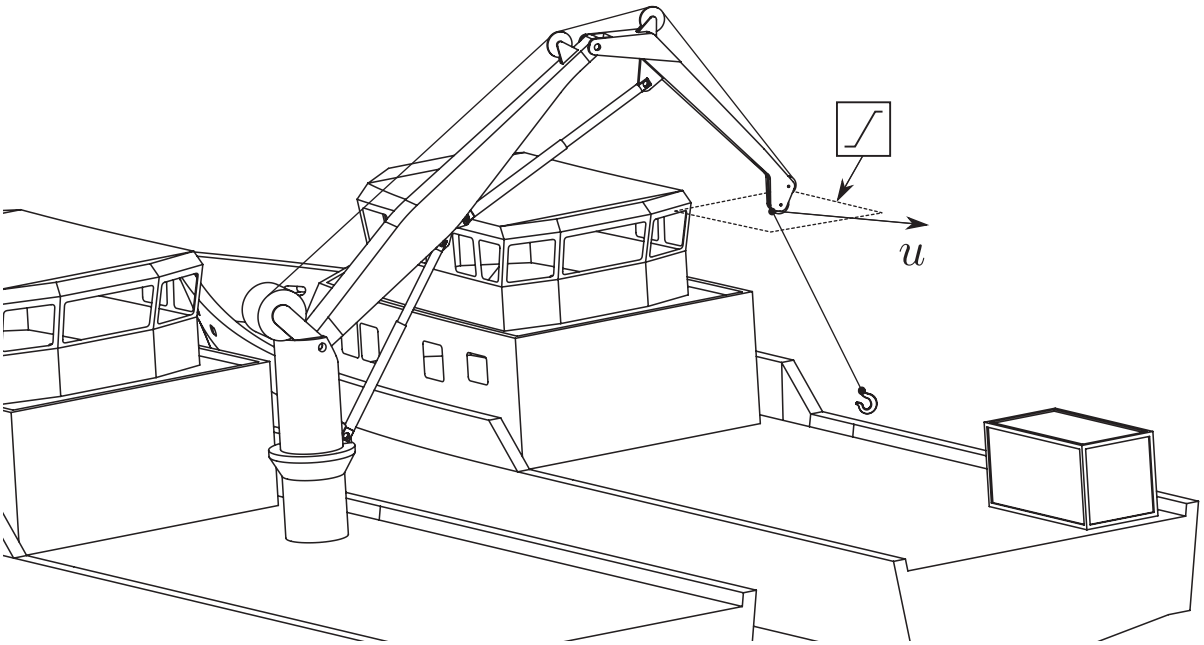

Figure 2.14: Illustration of the bounding box which the anti-swing assistant can use to dampen out the suspend load motion by using the control input $\boldsymbol{u}$ which again is integrated twice to form the additional input reference $\boldsymbol{r}_p$.

Figure 2.14 illustrates the control task to be carried out, where the crane tip move-

ment should be utilized to actively dampen out the swing motion of the suspended load. The control input $\boldsymbol{u}$ represents the desired acceleration at the crane tip in the heading coordinate system $\{n_1\}$. It is also shown in the figure that the crane has a restrained operational space, meaning that the anti-swing reference $\boldsymbol{r}_p$ has to be constrained to be within this allowable operation space, hence illustrated using the saturation block in both Figures 2.13 and 2.14. To realize this control task, the generated trajectory is therefore augmented with the observed swing angles and velocities as:

$$\boldsymbol{x} = \begin{bmatrix} \boldsymbol{p} \\ \dot{\boldsymbol{p}} \\ \boldsymbol{\varphi} \\ \dot{\boldsymbol{\varphi}} \end{bmatrix} = \begin{bmatrix} \boldsymbol{r}_p \\ \boldsymbol{\varphi} \\ \dot{\boldsymbol{\varphi}} \end{bmatrix} \tag{2.85}$$

which means that a state feedback controller can be used to minimize the following control task:

$$\lim_{t \to \infty} \boldsymbol{x} \to \boldsymbol{0} \tag{2.86}$$

i.e. the pendulum is hanging straight down and the additional reference input $\boldsymbol{r}_p$ is zero. The state feedback law:

$$\boldsymbol{u} = -\boldsymbol{K}\boldsymbol{x} \tag{2.87}$$

has to be tuned to meet the dynamic performance of the crane. As mentioned before, the crane dynamics are very complex and assumed to not be known, meaning that an accurate model of the crane can not be utilized to design the state feedback gain. In addition, using a simplified model which does not account for the crane dynamics will make the developed anti-swing assistant more modular and hence easier to retrofit to various crane types i.e. the plant is simply modeled as:

$$\boldsymbol{f}(\boldsymbol{x}, \boldsymbol{u}) = \begin{bmatrix} \dot{\boldsymbol{p}} \\ \boldsymbol{u} \\ \dot{\boldsymbol{\varphi}} \\ \boldsymbol{f}_{\text{load}}(\boldsymbol{\varphi}, \dot{\boldsymbol{\varphi}}, L_{w,0}, \dot{L}_{w,0}, c, g, [u_x, u_y, 0]^T) \end{bmatrix} \tag{2.88}$$

where $L_{w,0}$ and $\dot{L}_{w,0}$ are the wire length and velocity which represent the closest fit to the expected values during ship-to-ship operation. If theses values change a lot, one could consider adding a gain scheduling to the controller to solve this issue. The state feedback gain $\boldsymbol{K}$ is found from applying the LQR tuning principle minimizing the infinite time horizon LQR cost function:

$$J = \int_0^\infty \boldsymbol{x}^T \boldsymbol{Q} \boldsymbol{x} + \boldsymbol{u}^T \boldsymbol{R} \boldsymbol{u} \ dt \tag{2.89}$$

which finally will determine the optimal state feedback gain $\boldsymbol{K}$. The cost function has two weighting matrices, $\boldsymbol{Q}$ and $\boldsymbol{R}$ which have to be designed properly to meet the dynamic performance of the crane. The tuning principle is based on the idea of knowing some of the crane capabilities in terms of maximum velocity and acceleration in the crane tip,

which is assumed to be given by the crane manufacturer. By using these parameters, the two weighting matrices can be modeled as:

$$\boldsymbol{Q} = \begin{bmatrix} \frac{1}{p_{\max}^2}\boldsymbol{I}_{2\times 2} & \boldsymbol{0}_{2\times 2} & \boldsymbol{0}_{2\times 2} & \boldsymbol{0}_{2\times 2} \\ \boldsymbol{0}_{2\times 2} & \frac{1}{\dot{p}_{\max}^2}\boldsymbol{I}_{2\times 2} & \boldsymbol{0}_{2\times 2} & \boldsymbol{0}_{2\times 2} \\ \boldsymbol{0}_{2\times 2} & \boldsymbol{0}_{2\times 2} & \frac{1}{\varphi_{\max}^2}\boldsymbol{I}_{2\times 2} & \boldsymbol{0}_{2\times 2} \\ \boldsymbol{0}_{2\times 2} & \boldsymbol{0}_{2\times 2} & \boldsymbol{0}_{2\times 2} & \frac{1}{\dot{\varphi}_{\max}^2}\boldsymbol{I}_{2\times 2} \end{bmatrix}, \quad \text{and} \quad \boldsymbol{R} = \frac{1}{u_{\max}^2}\boldsymbol{I}_{2\times 2} \tag{2.90}$$

where the maximum "accepted" error in the state vector, and the control input is tuned to not violate the crane dynamics given by the crane manufacturer. This tuning principle is motivated from [53], where a similar approach was used to determine the diagonal weights of the weighting matrices. Using this tuning principle, smaller maximum crane tip acceleration will make the controller act much less aggressively to dampen out the load motions, since smaller values for $u_{\max}$ will cause higher values in $\boldsymbol{R}$ and hence the cost contribution of the input $\boldsymbol{u}$ will contribute more to the optimization cost given by Eq. 2.89.

Given that some suitable values for $\boldsymbol{Q}$ and $\boldsymbol{R}$ are derived, the LQR cost function is to be minimized and the state feedback gain:

$$\boldsymbol{K} = \boldsymbol{R}^{-1}\boldsymbol{B}^{\boldsymbol{T}}\boldsymbol{P} \tag{2.91}$$

is to be calculated, where $\boldsymbol{P}$ is found from solving the algebraic Ricatti equation:

$$\boldsymbol{A}^T\boldsymbol{P} + \boldsymbol{P}\boldsymbol{A} - \boldsymbol{P}\boldsymbol{B}\boldsymbol{R}^{-1}\boldsymbol{B}^T\boldsymbol{P} + \boldsymbol{Q}. \tag{2.92}$$

which is the optimal solution to the LQR cost function given by Eq. 2.89. The algebraic Ricatti equation implies that the linear model matrices $\boldsymbol{A}$ and $\boldsymbol{B}$ are known for our plant, hence a linearization of the non-linear state-space model given by Eq. 2.88 is required. The non-linear plant is linearized according to:

$$\boldsymbol{A} = \left.\frac{\partial \boldsymbol{f}(\boldsymbol{x},\boldsymbol{u})}{\partial \boldsymbol{x}}\right|_{\boldsymbol{x}_0,\boldsymbol{u}_0} \quad \text{and} \quad \boldsymbol{B} = \left.\frac{\partial \boldsymbol{f}(\boldsymbol{x},\boldsymbol{u})}{\partial \boldsymbol{u}}\right|_{\boldsymbol{x}_0,\boldsymbol{u}_0} \tag{2.93}$$

where $(\boldsymbol{x}_0, \boldsymbol{u}_0)$ is the linearization point which should be as close to the operation point as possible. Since the pendulum is mostly hanging almost directly downwards, the point of linearization is chosen to be zero for both the state vector and the input vector.

Another approach to tune the state feedback gain is to model the crane tip dynamics i.e. a transfer function relating the control input $\boldsymbol{u}$ and the actual acceleration $\ddot{\boldsymbol{r}}_{t/n_1}^{n_1}$ using a linear model. This approximate dynamic model could have been found from experimental system identification methods. However, this has not been investigated in this project, but it is believed to further improve the control performance compared to the one presented here.

2.6.3.5 Experimental Results

To verify the effectiveness of applying the crane operator assistant system presented in Section 2.6, The Norwegian Motion Laboratory has been used as an experimental testbed

like with all the appended papers. The Qualisys system has been used to measure the hook motion in real-time since this system was already available and operational in the lab setup. Other methods to track the hook could have been applied, such as vision or point cloud detections to mention only some potential candidates. The swing motion was estimated in real-time using the load EKF presented in Section 2.6.3.3. To observe the relative motion between the two Stewart platforms, the ship-to-ship EKF described in Section 2.5 was used.

Various experiments could have been conducted to investigate the effectiveness of the proposed crane operator assisting system. However, an experiment where the wire length assistant is activated throughout the whole test sequence, and the anti-swing assistant was activated after 20s was used to verify the effectiveness of the proposed solution. As mentioned previously in the introduction, the safety is an important factor when it comes to landing a load on the ship deck of the second ship. Using energy considerations, a measure of the reduced risk can be investigated by measuring the relative velocity between the transferred load and a fixed location on the second ship deck, where the resulting kinetic energy of the load is calculated as:

$$E_k = \frac{1}{2} m_L \boldsymbol{v}^T \boldsymbol{v} \tag{2.94}$$

where the relative velocity $\boldsymbol{v}$ is calculated from using the high precision internal feedback sensors of the lab equipment which have been calibrated in Paper H to yield high precision. The overall effectiveness and the increased safety due to the reduced energy in the suspended load are illustrated by Figure 2.15.

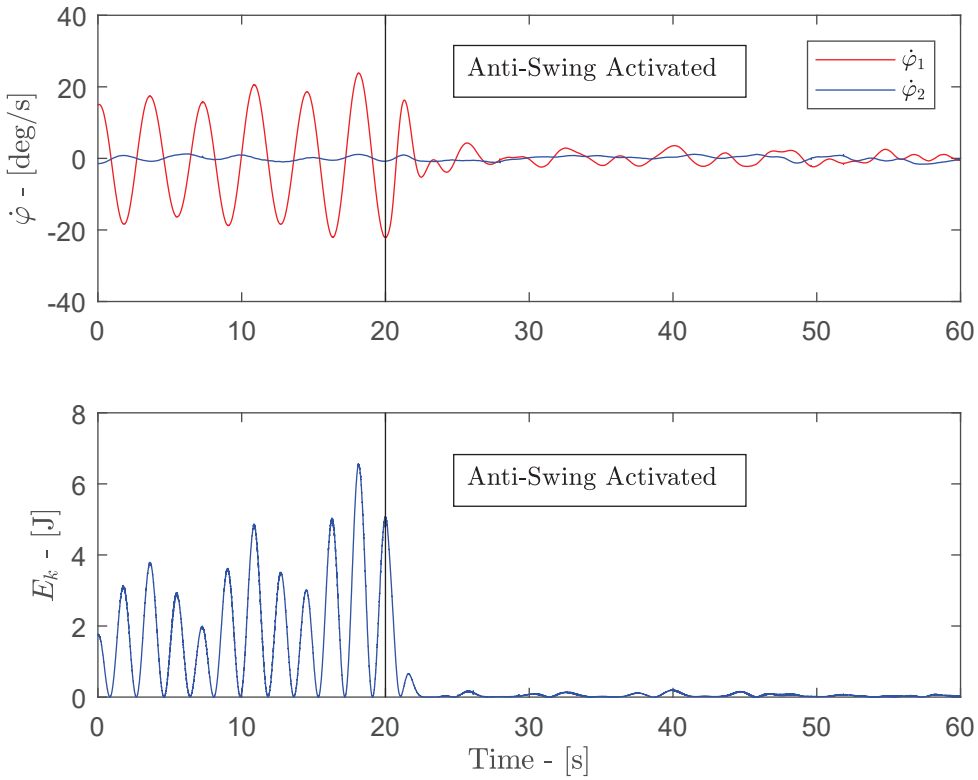

Figure 2.15: Illustration of the load swing velocities and the reduced kinetic energy of the suspended load due to the activated anti-swing assistant ($m_L = 10kg$).

The figure clearly indicates that the angular velocities of the suspended load are reduced drastically when the anti-swing assistant is activated compared to when deactivated. As a result, the kinetic energy is reduced accordingly and hence the operation can be seen as much safer since any collision would be less severe in case of impact. To quantify the reduced energy illustrated in Figure 2.15, the mean energy before and after $t = 20s$ are calculated according to:

$$\bar{R}_I = \frac{\mu(0,20)}{\mu(20,60)} = 16.2, \quad \text{where} \quad \mu(a,b) = \frac{1}{b-a}\int_a^b E_k(t)dt \tag{2.95}$$

where $\bar{R}_I$ is the ratio of averaged reduced impact energy due to the activated anti-swing assisting system. Another important factor is the increased precision of the load handling itself. Due to the less swinging motion and the automatic adjustment of the wire length using the winch, the crane operator should be able to place the load with higher precision than without the assistants active.

The anti-swing assistant presented in Section 2.6.3 utilized the presented LQR state feedback controller to minimize the swing motion while at the same time also minimizing its own control input. In other words, the additional control input from the anti-swing assistant should always try to go back to zero i.e. the desired position described by the crane operator input is reached. This effect is demonstrated by Figure 2.16 where the "maximum" values used to design the $\boldsymbol{Q}$ and $\boldsymbol{R}$ weighting matrices are indicated with the black stapled lines.

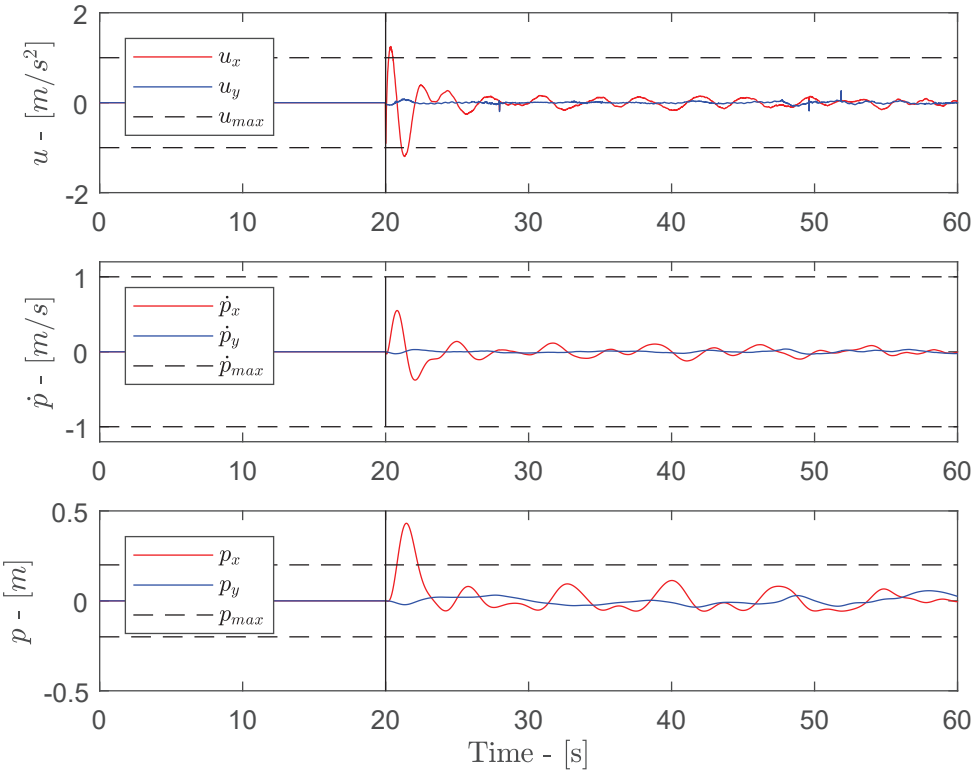

Figure 2.16: The anti-swing control input $\boldsymbol{u}$ and the integrated velocity $\dot{\boldsymbol{p}}$ and position $\boldsymbol{p}$ used to create the correcting input needed to dampen out the load swing motion. The black stapled lines represent the values used to design the LQR weighting matrices $\boldsymbol{Q}$ and $\boldsymbol{R}$.

The experiment demonstrates that the LQR input $\boldsymbol{u}$ and the correction trajectory $\boldsymbol{r}_p$ is more or less kept within the prescribed "maximum" values used to tune the LQR state feedback gain. However, this experiment was carried out at the very end of this project and further investigation of the proposed solution is needed, especially in relation to an offshore crane featuring slower dynamics compared to the industrial robot used for this experiment. Two videos showing the experimental results have been published at YouTube, `https://www.youtube.com/watch?v=cX2pjp69kSQ` and `https://www.youtube.com/watch?v=ens4hbkdDMo`.

Chapter 3

Concluding Remarks

3.1 Conclusions

The work presented in this thesis and the appended papers have been devoted to the investigation of the ship-to-ship load handling scenario, where the goal is to transfer a load from one ship onto another while situated at sea. This task requires the relative ship motion to be measured or observed in real-time, and hence a novel ship-to-ship state estimation algorithm has been developed using the accompanying ship-to-ship kinematics. The presented EKF algorithm combined inertial, visual, time-of-flight, and/or satellite navigation sensors to observe the relative ship motions in real-time. Redundancy is often required in offshore operations, and hence the proposed method is designed in such a manner that the relative ship motion can be estimated using only the two MRUs for smaller time periods. Placing an MRU on each ship will imply that the second MRU data has to be transferred to the main ship using a wireless communication link. This capability has been experimentally investigated using an off-the-shelf radio link where the typical time delay was found to be 8ms, which is considered to be more than sufficient considering the slow ship motions.

A novel kinematic control system aimed at assisting the crane operator while transferring the load onto the second ship was developed at the end of this project. This crane operator assistant consists of two separate systems; the wire-length assistant and the anti-swing assistant. The wire-length assistant makes use of the ship-to-ship EKF algorithm and the crane kinematics to calculate the wire length which will keep the transferred load in a fixed distance above the second ship deck. The anti-swing assistant reduced the load swing motion by manipulating the crane tip based on the observed load motion. The proposed method was experimentally investigated in the lab setup, where the average impact energy in case of a collision was reduced with a factor of 16.2. The crane dynamics were not modeled in detail when designing the kinematic controller, which is motivated by the desire of developing a modular system which can be retrofitted on already existing cranes with proprietary control systems. An LQR state feedback controller was used to generate the crane tip trajectory needed to dampen out the load swing motion, where the maximum acceleration and velocity of the crane tip was used to calculate the state feedback gain.

Even though the extensive development of the Norwegian Motion Laboratory is not

considered part of the scientific contribution of this thesis, the lab development has been an absolute necessity in achieving the experimental results presented in this thesis and the appended papers. The lab development phases have also given valuable insight in understanding the challenges of using real sensors and machines in terms of their limitations. These limitations are not always evident or considered when working with simulation models, and hence not considered when designing the state estimators and the control algorithms. It is therefore in the author's belief that the developed control and estimation algorithms are more suitable of being realized in a real ship-to-ship scenario compared to algorithms designed on the basis of simulation models only.

The experimental study of this project demonstrates the increased potential in terms of repeatability and safety of future ship-to-ship operations. It is therefore expected that the weather window could be further increased if the presented methods are retrofitted or made available with new cranes in the future. The author of this thesis has experienced an increased interest from several offshore companies in relation to the methods developed and presented in this thesis. After the submission of this thesis, the author will continue the development of the methods for implementation on heavy offshore cranes in one of the partner companies of the SFI Offshore Mechatronics center.

3.2 Future Work

The conclusion mentioned that the dynamic performance of the industrial robot is not comparable with an offshore crane, especially in terms of speed and repeatability. A study where the developed anti-swing assistant is implemented on an offshore crane, either using a simulation or even a real crane should be carried out to validate the proposed method for use with an offshore crane. In addition, an investigation of controlling the wire length instead of the crane tip to reduce the swing motion should be investigated using an energy-based approach where the stability could be proved using Lyapunov methods.

It has also been assumed in this work that the hook motion could be measured, and hence the suspended load angles are observed for use in the anti-swing system, which is why a robust sensor capable of measuring the hook motion needs further investigation. It is believed that a combination of both vision and a time-of-flight sensor could be used to measure the hook motion in real-time, but this has to be investigated experimentally. It may also be evident from such a study that this sensor system is found to be accurate enough to detect the cargo deck of the second ship, and hence may remove the need for a second MRU and a wireless communication link as presented in this thesis. If this scenario is true, the presented ship-to-ship kinematics are still valuable information for future algorithm development using other sensor setups like the one mentioned.

In order to quantitatively assess the potentially increased safety and weather window for ship-to-ship load transfer operations, further simulation studies are required where typically heavy offshore cranes are considered instead of an industrial robot. The increase in weather window depends among other factors on the dynamic performance of the offshore crane, disturbances from wind forces, the size and the weight of the transferred load, and industry regulations from contractors and certification agencies.

Bibliography

[1] MacGregor AHC Crane. `http://maritimt.com/sites/default/files/article/images/macgregor-300414.jpg`. Accessed: 2018-09-17.

[2] Barge Master T40 Crane Image. `https://www.barge-master.com/fileadmin/_processed_/7/0/csm_Slideshow_image_2_e04a803d62.jpg`. Accessed: 2018-09-17.

[3] M. B. Kjelland. *Offshore Wind Turbine Access Using Knuckle Boom Cranes*. PhD thesis, University of Agder, Grimstad, Norway, 2016.

[4] Esa J., Jonne P., Risto J., and Jouni S. Remote and autonomous ships: The next steps. AAWA Position Paper, Rolls Royce plc, London, 88 pages., June 2016.

[5] J.-M. Godhaven. Adaptive tuning of heave filter in motion sensor. In *IEEE Oceanic Engineering Society. OCEANS'98. Conference Proceedings, Nice, France*, pages 174–178, 1998. doi: 10.1109/OCEANS.1998.725731.

[6] S. Küchler, C. Pregizer, J. K. Eberharter, K. Schneider, and O. Sawodny. Real-time estimation of a ship's attitude. In *American Control Conference (ACC), San Francisco, CA, USA*, pages 2411–2416. IEEE, 2011. doi: 10.1109/ACC.2011.5990612.

[7] M. Richter, K. Schneider, D. Walser, and O. Sawodny. Real-time heave motion estimation using adaptive filtering techniques. *IFAC Proceedings Volumes*, 47(3):10119–10125, 2014. doi: 10.3182/20140824-6-ZA-1003.00111.

[8] S. Küchler, J. K. Eberharter, K. Langer, K. Schneider, and O. Sawodny. Heave motion estimation of a vessel using acceleration measurements. *IFAC Proceedings Volumes*, 44(1), 2011. doi: 10.3182/20110828-6-IT-1002.01935.

[9] T. H. Bryne, R. H. Rogne, T. I. Fossen, and T. A. Johansen. Attitude and heave estimation for ships using MEMS-based inertial measurements. *IFAC-PapersOnLine*, 49(23):568–575, 2016. doi: 10.1016/j.ifacol.2016.10.496.

[10] J. K. Woodacre, R. J. Bauer, and R. A. Irani. A review of vertical motion heave compensation systems. *Ocean Engineering*, 104:140–154, 2015. doi: 10.1016/j.oceaneng.2015.05.004.

[11] M. B. Kjelland, I. Tyapin, G. Hovland, and M. R. Hansen. Tool-point control for a redundant heave compensated hydraulic manipulator, 2012. doi: 10.3182/20120531-2-NO-4020.00034.

[12] J. Neupert, T. Mahl, B. Haessig, O. Sawodny, and K. Schneider. A heave compensation approach for offshore cranes. In *IEEE American Control Conference, Seattle, Washington, USA*, pages 538–543, 2008. doi: 10.1109/ACC.2008.4586547.

[13] S. Küchler, T. Mahl, J. Neupert, K. Schneider, and O. Sawodny. Active control for an offshore crane using prediction of the vessel's motion. *IEEE/ASME Transactions on Mechatronics*, 16(2):297–309, 2011. doi: 10.1109/TMECH.2010.2041933.

[14] S. Messineo and A. Serrani. Offshore crane control based on adaptive external models. *Automatica*, 45(11):2546–2556, 2009. doi: 10.1016/j.automatica.2009.07.032.

[15] T. A. Johansen, T. I. Fossen, and F. G. Sagatun, S. I.and Nielsen. Wave synchronizing crane control during water entry in offshore moonpool operations-experimental results. *IEEE Journal of Oceanic Engineering*, 28(4):720–728, 2003.

[16] YouTube, MacGregor three-axis motion compensation offshore crane. `https://www.youtube.com/watch?v=oVs4GhjZrbk&t=39s`.

[17] YouTube, Barge Master T40 Animation. `https://www.youtube.com/watch?v=vE8_aE1DRtk`.

[18] YouTube, MacGregor Ship-to-Ship Compensation System. `https://www.youtube.com/watch?v=5_QoSTrU2gc`.

[19] YouTube, NOV Sealift Compensation System. `https://www.youtube.com/watch?v=oJHl6g9R6z8`.

[20] E. Lataire, M. Vantorre, and G. Delefortrie. Captive model testing for ship to ship operations. In *International Conference on Marine Simulation and Ship Maneuverability (MARSIM'09), Panama City, Panama*, 2009.

[21] E. Lataire, M. Vantorre, J. Vandenbroucke, and K. Eloot. Ship to ship interaction forces during lightering operations. In *2nd International Conference on Ship Manoeuvring in Shallow and Confined Water: Ship to ship interaction, Trondheim, Norway*, pages 211–222. Royal Institution of Naval Architects, 2011.

[22] Loss Prevention Briefing, Ship to Ship Transfer Operations, North of England P&I Association. `http://www.nepia.com/media/869603/Ship-to-Ship-Transfer-LP-Briefing.PDF`, 2015.

[23] Ship to Ship Transfers - Considerations Applicable to Reverse Lightering Operations, Oil Companies International Marine Forum. `https://www.ocimf.org/media/8922/935be10f-7be0-4c00-b479-4c4e4b77ce89.pdf`, 2009.

[24] Ship to Ship Transfers - Port of Gothenburg, The Port of Scandinavia. `https://www.goteborgshamn.se/FileDownload/?contentReferenceID=13816`.

[25] L. S. McTamaney and F. P. Haley. Ship-to-ship fluid transfer system, 1983. US Patent 4,408,943.

[26] D. R. Garrett and D. F. Preston. Ship to ship refueling device, 1965. US Patent 3,199,553.

[27] L. Ramli, Z. Mohamed, A. M. Abdullahi, H. I. Jaafar, and I. M. Lazim. Control strategies for crane systems: A comprehensive review. *Mechanical Systems and Signal Processing*, 95:1–23, Oct 2017. doi: 10.1016/j.ymssp.2017.03.015.

[28] L. A. Tuan, S.-C. Moon, W. G. Lee, and S.-G. Lee. Adaptive sliding mode control of overhead cranes with varying cable length. *Journal of Mechanical Science and Technology*, 27(3):885–893, 2013. doi: 10.1007/s12206-013-0204-x.

[29] N. B. Almutairi and M. Zribi. Sliding mode control of a three-dimensional overhead crane. *Journal of Vibration and Control*, 15(11):1679–1730, 2009. doi: 10.1177/1077546309105095.

[30] R. M. T. R. Ismail and Q. P. Ha. Trajectory tracking and anti-sway control of three-dimensional offshore boom cranes using second-order sliding modes. In *IEEE International Conference on Automation Science and Engineering (CASE), Wisconsin, USA*, pages 996–1001. IEEE, 2013. doi: 10.1109/CoASE.2013.6654071.

[31] R. M. T. R. Ismail, N. D. That, and Q. P. Ha. Offshore container crane systems with robust optimal sliding mode control. In *31st International Symposium on Automation and Robotics in Construction and Mining, ISARC, Sydney, Australia*, 2014.

[32] L. A. Tuan, S.-G. Lee, V.-H. Dang, S. Moon, and B. S. Kim. Partial feedback linearization control of a three-dimensional overhead crane. *International Journal of Control, Automation and Systems*, 11(4):718–727, Aug 2013. doi: 10.1007/s12555-012-9305-z.

[33] N. Sun and Y. Fang. New energy analytical results for the regulation of underactuated overhead cranes: An end-effector motion-based approach. *IEEE Transactions on Industrial Electronics*, 59(12):4723–4734, 2012. doi: 10.1109/TIE.2012.2183837.

[34] Y. Chu, F. Sanfilippo, V. Æsøy, and H. Zhang. An effective heave compensation and anti-sway control approach for offshore hydraulic crane operations. In *IEEE International Conference on Mechatronics and Automation, Tianjin, China*, pages 1282–1287. IEEE, 2014. doi: 10.1109/ICMA.2014.6885884.

[35] T. I. Fossen. *Handbook of Marine Craft Hydrodynamics and Motion Control*. John Wiley & Sons Ltd., 2011.

[36] T. I. Fossen and T. Perez. Marine Systems Simulator (MSS). `https://github.com/cybergalactic/MSS`. Accessed: 2018-10-23.

[37] T. I. Fossen. Description of MSS vessel models: Configuration guidelines for hydrodynamic codes. `http://www.marinecontrol.org/pdf/2008_06_19_MSS_vessel_models.pdf`, 2008. Accessed: 2018-10-23.

[38] T. Perez, Ø. N. Smogeli, T. I. Fossen, and A. J. Sørensen. An overview of the marine systems simulator (MSS): A simulink toolbox for marine control systems. *Journal of Modeling, identification and Control*, 27(4):259–275, 2006.

[39] W. J. Pierson Jr. and L. Moskowitz. A proposed spectral form for fully developed wind seas based on the similarity theory of S. A. Kitaigorodskii. *Journal of Geophysical Research*, 69(24):5181–5190, 1964. doi: 10.1029/JZ069i024p05181.

[40] Q. Guo and Z. Xu. Simulation of deep-water waves based on JONSWAP spectrum and realization by MATLAB. In *19th International Conference on Geoinformatics, IEEE, Shanghai, China*, 2011. doi: 10.1109/GeoInformatics.2011.5981100.

[41] A. J. Sørensen. A survey of dynamic positioning control systems. *Annual Reviews in Control*, 35(1):123–136, 2011. doi: 10.1016/j.arcontrol.2011.03.008.

[42] M. J. Grimble, R. J. Patton, and D. A Wise. The design of dynamic ship positioning control systems using stochastic optimal control theory. *Optimal Control Applications and Methods*, 1(2):167–202, 1980. doi: 10.1002/oca.4660010207.

[43] K. Y. Pettersen and T. I. Fossen. Underactuated dynamic positioning of a ship-experimental results. *IEEE Control Systems Society*, 8(5):856–863, 2000. doi: 10.1109/87.865859.

[44] J. Denavit and R. S. Hartenberg. A kinematic notation for lower-pair mechanisms based on matrices. *ASME Journal of Applied Mechanics*, 22:215–221, 1955.

[45] R. S. Hartenberg and J. Denavit. *Kinematic Synthesis of Linkages*. McGraw-Hill, 1964.

[46] M. W. Spong, S. Hutchinson, and M. Vidyasagar. *Robot Modeling and Control*. John Wiley and Sons, 2006.

[47] O Øvstedal, N. S. Kjørsvik, and J. G. O. Gjevestad. Surveying using gps precise point positioning. In *XXII International FIG Congress, Munich, Germany*, page 10, 2006.

[48] O. Chassagne. One-centimeter accuracy with PPP. *Inside GNSS*, pages 49–54, 2012.

[49] O. Gjelstenli. Anti-sway control and wave following system for offshore lattice crane, 2012.

[50] T. A. Myhre and O. Egeland. Tracking a swinging target with a robot manipulator using visual sensing. *Journal of Modeling, Identification and Control*, 37(1):53–62, 2016. doi: 10.1109/IECON.2016.7793396.

[51] T. A. Myhre and O. Egeland. Estimation of crane load parameters during tracking using expectation-maximization. In *IEEE American Control Conference (ACC), Seattle, WA, USA*, pages 4556–4562. IEEE, 2017. doi: 10.23919/ACC.2017.7963658.

[52] H. Ouyang, N. Uchiyama, and S. Sano. Suppression of two-dimensional load-sway in rotary crane control using only horizontal boom motion. *Journal of System Design and Dynamics*, 5(4):535–546, 2011. doi: 10.1299/jsdd.5.535.

[53] R. M. Murray. CDS 110b Lecture 2 - LQR Control. `http://www.cds.caltech.edu/~murray/courses/cds110/wi06/L2-1_LQR.pdf`, 2006.